

Frequency Control and Stabilization of a Laser System

Chu Cheyenne Teng

Advisor: Professor David A. Hanneke
December 10, 2013

Submitted to the
Department of Physics of Amherst College
in partial fulfilment of the
requirements for the degree of
Bachelors of Arts with honors

© 2013 Chu Cheyenne Teng

Abstract

Quantum logic spectroscopy enables state manipulation and precise spectral measurement of many charged atoms and molecules. One application of this technique is precise spectroscopy of molecules, which can improve searches for the time variation of the proton-electron mass ratio (μ). By co-trapping the molecular ion with an atomic ion, the two ions are coupled through the Coulomb interactions. Because of this, the cooling and internal state preparation of an atomic ion, in our case ${}^9\text{Be}^+$, are extended to the molecular ion.

My thesis describes the construction of a stable and versatile laser system for efficient cooling, state preparation, and detection of ${}^9\text{Be}^+$. We demonstrate a laser lock that transfers the frequency stability of a helium-neon laser to less stable lasers using a Fabry-Perot cavity. An external frequency reference, provided by a thallium fluoride molecular transition, shows that the system is stable to within 200 kHz over 3 hours. We also performed injection current modulation on an external cavity diode laser in order to produce a frequency detuning critical for the cooling scheme. The current setup can achieve a maximum modulation frequency of 6.6 GHz with 3% of the output power in an optical sideband.

Acknowledgments

Professor Hanneke, thank you. In the past two years, you have been a most resourceful and passionate mentor to me. The weekly meetings that were once intimidating, and at times confusing, have actually turned into something I enjoy and look forward to—it's true!

Thank you, my physics professors. You have always been available and supportive. A major part of my Amherst experience consists of you, and I am thankful and happy for that.

A special thanks to the Friedman Lab, for generously lending me the rf generator. It is critical for half of my thesis. Thank you Steve Peck, for your company in lab over the summer and your powerful Labview skill. And Jim Kubasek, my thesis would not have been possible without you.

To my labmates and my friends, I have said little in the past, but I feel so lucky to have known you and spent time with you.

I am grateful for the generous support from the Amherst College Dean of the Faculty, National Science Foundation, and the Research Corporation for Science Advancement.

Last but not least, I am most fortunate to have my sweet family. Mom, Dad, and Cavell, thank you for your patience, support, and love.

Contents

1	Introduction	1
1.1	Why Beryllium Ion?	3
1.2	Internal State Preparation and Detection	4
1.3	Doppler Cooling	6
1.4	Resolved Sideband Cooling	7
1.4.1	Stimulated Raman Transitions	7
1.4.2	Laser Repumping	9
1.5	An Overview	10
2	Frequency Stabilization: The Scanning Fabry-Perot Cavity	12
2.1	System Setup	13
2.2	The Confocal Fabry-Perot Cavity	15
2.2.1	The Basic Theory	16
2.2.2	Athermal Cavity Design	20
2.2.3	Obtaining the Confocal Condition	25
2.3	The External Cavity Diode Laser	27
2.3.1	The Diffraction Grating	30
2.4	System Performance	32
2.4.1	System Stability	32
2.4.2	Reaction to Temperature Drifts	36
2.4.3	The Other Factors	38
3	Injection Current Modulation	40
3.1	Experimental Setup	41
3.2	Supporting Theory	42
3.2.1	$p - n$ Junctions	42
3.2.2	Radiative and Non-radiative Mechanisms	44
3.2.3	The Rate Equations	45
3.2.4	The AM Theory	49
3.2.5	The FM Theory	50

3.2.6	Optical Sidebands	51
3.3	Experimental Observations	54
3.3.1	General Decline with Increasing Modulation Frequency	57
3.3.2	Dramatic Improvements from External Cavity Feedback	60
3.3.3	Bias Current Dependence	61
3.3.4	Frequency of Oscillation Relaxations	63
3.3.5	Mysterious Sidebands	65
4	Conclusion	68
A	Optical Sideband Derivations	70
B	Allan Deviation	73

List of Figures

1.1	Energy Level Diagram for ${}^9\text{Be}^+$	4
1.2	Stimulated Raman Transitions	8
1.3	Required Lasers	11
2.1	F-P System Setup	13
2.2	DAQ Analog I/O	15
2.3	F-P Cavity Beam Path	16
2.4	Cartoon of The F-P Cavity	20
2.5	Demonstration of the Radius of Curvature	23
2.6	Cartoon of The F-P Cavity	23
2.7	F-P System Photos	24
2.8	Photo of Complete Setup	25
2.9	Single HeNe Transmission Peak	26
2.10	Multiple HeNe Transmission Peaks	28
2.11	ECDL photo	29
2.12	Diffraction Grating Illustration	30
2.13	TIF Transition Peak	33
2.14	System Stability Over 3 Hours	34
2.15	Laser Frequency Unlocked	35
2.16	Allan Deviation Plot	36
2.17	Frequency vs. Temperature	37
2.18	Laser Power Drift	38
2.19	Channel A/Channel B	39
3.1	Injection Current Modulation Setup	41
3.2	$p - n$ Junction	43
3.3	Stimulated Emission	44
3.4	Bessel Functions	53
3.5	Sideband Patterns	55
3.6	Coincident First Sidebands	56
3.7	Sideband Illustration	57

3.8	Reflected RF Power	58
3.9	Modulation Depth	59
3.10	Modulation Indices	60
3.11	Bias Current Dependence at 4300 MHz (Modulation Depth)	62
3.12	Bias Current Dependence at 4300 MHz (Modulation Indices)	63
3.13	Bias Current Dependence at 6644 MHz (Modulation Indices)	64
3.14	Bias Current Dependence at 6644 MHz (Modulation Depth)	64
3.15	Unexpected Sidebands	66

Chapter 1

Introduction

We plan to build a system capable of performing spectroscopy on a variety of charged species. Such a system will be a versatile tool for studying species whose more complicated structures previously hindered precise spectral measurements. A useful application of this system is to measure the time variation of the proton-electron mass ratio (μ) using molecules. Since several physical theories seeking to unify general relativity with quantum mechanics predict that μ changes over time, more sensitive measurements of $d\mu/dt$, which this setup can potentially offer, can serve to confirm or disprove these theories.[1]

In contrast to atoms, molecules lack the structural simplicity that allows for effective cooling and internal state preparation. This is why despite having energy transitions that are more sensitive to variations in μ than atoms, molecular spectroscopy has not been a popular choice for measuring $d\mu/dt$. Our goal is to take advantage of the more sensitive spectroscopy transitions in molecules while exploiting the favorable features of the atoms using quantum logic spectroscopy.

We realize quantum logic spectroscopy in three steps. First, we co-trap a diatomic molecular ion (designated the spectroscopy ion) with an atomic ion (designated the logic ion) in a linear Paul trap designed by Shenglan Qiao.[2] Second, the spectroscopy ion is sympathetically cooled to its translational ground state because of the motional coupling between the two ions through Coulomb interactions.¹ The spectroscopy ion is then further cooled to its rotational ground state without disturbing its translational and vibrational states. Third, we manipulate the internal states of the spectroscopy ion in order to measure the desired transition frequency. We are currently constructing the apparatus for the first two steps.

My thesis focuses on the second step, where a stable laser system is required for sympathetic cooling and state initialization. In this thesis, I demonstrate a frequency lock that stabilizes the frequency of the lasing source, which is an external cavity diode laser (ECDL). I also show that injection current modulation of the ECDL is a convenient and viable method that allows us to obtain all of the required laser frequencies from the ECDL.²

For the rest of this chapter, I first discuss the reasons behind our choice of the logic ion, ${}^9\text{Be}^+$, in Sec. 1.1. Then I provide some details about the cooling methods that we plan to use—Doppler cooling and resolved sideband cooling. The implementation of the cooling scheme will directly motivate the rest of this thesis.

¹In room temperature, the molecules are mostly in their vibrational ground states.

²The ECDL provides a laser beam at 940nm, which is converted into 313nm using the setup designed by Celia Ou.[3] Note that frequency conversion happens after injection current modulation and both the original ECDL output and the modulated output are frequency converted with the frequency difference between them preserved.

1.1 Why Beryllium Ion?

Since quantum logic spectroscopy relies on the Coulomb interaction between the logic ion and the spectroscopy ion, ${}^9\text{Be}^+$ satisfies the very first criterion: being an ion. With a single valence electron, ${}^9\text{Be}^+$ also has a simple and well-studied structure that makes it a popular choice for atomic trapping and cooling. It is also important that ${}^9\text{Be}^+$ has a nuclear spin $I = 3/2$. When subject to a magnetic field, the nuclear spin couples with the valence electron spin ($S = 1/2$) to form hyperfine structures. For effective atomic state manipulations, hyperfine structures are preferable because of their relatively large spectral splittings (1.25 GHz for the two hyperfine states we are interested in) and long decay times ($\sim 10^{15}s$). [4, p 13]

Fig. 1.1 shows the energy level diagram of a ${}^9\text{Be}^+$. The ground state has a total of 8 hyperfine states, which I show split under the influence of a magnetic field.³ The first excited states of ${}^9\text{Be}^+$ consist of the fine structure manifold due to spin-orbit coupling. Each of the resulting $P_{1/2}$ and $P_{3/2}$ states also has its own hyperfine structures: $P_{1/2}$ contains 8 hyperfine states and $P_{3/2}$ contains 16 hyperfine states. Note that the fine structure splitting between the two excited P states is 197 GHz. This large splitting allows us to safely ignore the $P_{1/2}$ states when we excite the atoms to the $P_{3/2}$ states.

We have designated $S_{1/2}|F = 2, m_F = 2\rangle$ to be $|\downarrow\rangle$ and $S_{1/2}|1, 1\rangle$ as $|\uparrow\rangle$, and the energy splitting between them corresponds to ~ 1.25 GHz. The reason for this labeling will become obvious when we discuss stimulated Raman transitions in Sec. 1.4.

³For $I = 3/2$ and $S = 1/2$, F can be either 1 or 2, and for each F we can have $2F + 1$ hyperfine states corresponding to each allowed m_F .

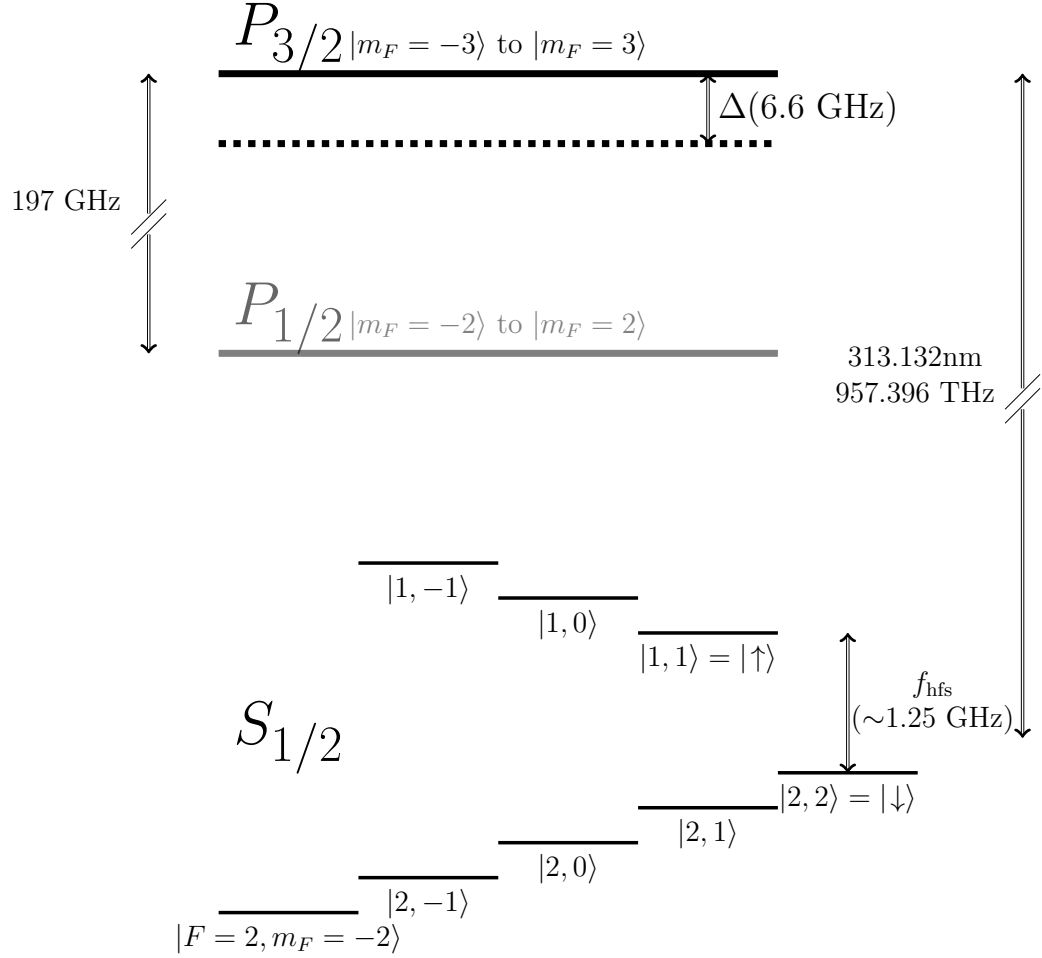


Figure 1.1: The energy level diagram for ${}^9\text{Be}^+$. The $S_{1/2}$ hyperfine manifold is illustrated. $P_{3/2}$ contains 16 hyperfine levels and the $P_{1/2}$ contains 8 hyperfine levels. The dashed line shows a detuning of 6.6 GHz from $P_{3/2}$, which will be used for Raman transitions.

1.2 Internal State Preparation and Detection

In order to reliably detect the internal state of the logic ions, we use a cycling transition that allows us to continuously observe scattered photons without disturbing the prepared atomic states. We choose the cycling transition between $S_{1/2}|2, 2\rangle$ and

$P_{3/2}|3, 3\rangle$. Once excited to the $P_{3/2}|3, 3\rangle$ state, the atoms can only decay back to $S_{1/2}|2, 2\rangle$ because the selection rule requires $\Delta m_F = \pm 1$ or 0, and there are no ground states with $m_F = 3$ or 4. Under a detection beam that is resonant with this cycling transition, the atoms are restricted to cycle only between these two states, leading to continuous spontaneous emissions.

It is important to make sure that the detection beam stays resonant with the cycling transition for accurate detection. Note that the linewidth of the $P_{3/2}|3, 3\rangle$ state is only 19.4 MHz. If the laser frequency drifts beyond this range, we no longer detect photons firstly because the laser is no longer resonant with the cycling transition, and secondly because it cannot drive any other atomic transitions due to its polarization. This is the principal reason for stabilizing our laser frequencies; the frequency stabilization scheme is discussed in Chapter 2.

To enable the cycling transition, we need to initiate ${}^9\text{Be}^+$ in the $S_{1/2}|2, 2\rangle$ state. Note that the atoms are distributed among the ground-state hyperfine manifold because excited states decay quickly. The Doppler beams that we will discuss in the following section address atoms in all of the ground states because they are detuned within the linewidth of the ground state. For now, we use the Doppler beams for optical pumping. Since the $S_{1/2}|2, 2\rangle$ state has the highest m_F among all of the hyperfine states in $S_{1/2}$, we use right circularly polarized (σ^+) Doppler beams because the selection rule requires that $\Delta m_F = +1$ for each excitation. Again by the selection rule, the excited atom can either decay to a state with the same m_F or a higher m_F in comparison to the original state before excitation. Eventually all of the atoms end up in $S_{1/2}|2, 2\rangle$, where they become resonant with the cycling transition.

1.3 Doppler Cooling

The Doppler beams mentioned in the previous section are named for their roles in Doppler cooling. Since quantum logic spectroscopy couples the motions of the spectroscopy ion and the logic ion, it is crucial to reduce the translational motion of the logic ions to a known ground state for efficient state manipulations.

In Doppler cooling, the laser is tuned to the red of the resonant frequency. In the frame of reference of an atom moving towards a laser beam, the laser appears blue-shifted due to Doppler shift. When the red-detuning of the laser matches with the amount of blue-shift that the atom perceives, the laser beam becomes resonant with the atom. The atom thus first absorbs a photon, then emits one due to spontaneous emission. While the absorbed photon has a definite momentum against the direction of the atom, the emitted photon has an average momentum of 0 due to the random direction of emission. The net momentum imparted on the atom causes the atom to lose kinetic energy, hence lowering its temperature.

In our experiment, we first use a Doppler beam detuned by a few hundred MHz to address atoms with a wide range of velocities. This prepares the atoms for finer coolings from a second, less detuned Doppler beam (by half the linewidth of the excited state) to complete Doppler cooling. While free-space experiments require three pairs of cooling beams to cool atoms traveling in all directions, our atoms are already confined to a harmonic potential well⁴. Because of this, a single Doppler beam can cool all three atomic motions provided some of the laser's propagation direction lies along each trap axis.

⁴Both the spectroscopy ions and the logic ions will be housed in a linear Paul trap. The potential within the trap is analogous to a harmonic well.

Note that although Doppler cooling is an efficient cooling method, it cannot lower the temperature of the atoms beyond the Doppler limit. This limit is due to the background heating from the very process of absorption and emission that enabled Doppler Cooling. To further cool the atoms to sub-Doppler temperatures, we need to use a second cooling method called resolved sideband cooling.

1.4 Resolved Sideband Cooling

In order to cool the atoms beyond the Doppler limit, we consider their quantized vibrational motions (labeled $|n\rangle$) due to the harmonic potential of the trap. Sub-Doppler cooling involves reducing the atoms to the lowest vibrational levels ($|n = 0\rangle$). We plan to achieve this in two steps. First we use stimulated Raman transitions to couple $|\downarrow, n\rangle$ with $|\uparrow, n - 1\rangle$. We then repump the atoms to $|\downarrow\rangle$ without exciting their vibrational motions. The goal is to repeat this process enough times to cool the atoms to $|\downarrow, 0\rangle$.

1.4.1 Stimulated Raman Transitions

The first step in resolved sideband cooling is to couple the vibrational states of $|\downarrow\rangle$ and $|\uparrow\rangle$ using stimulated Raman transitions. As Fig. 1.2 shows, the setup requires two laser beams that indirectly couple $|\downarrow, n\rangle$ and $|\uparrow, n - 1\rangle$ through a third, transient excited state far detuned from the actual excited state.

In stimulated Raman transitions, the atom absorbs a photon corresponding to the energy of one of the laser beams, then emits one with the same energy as the other laser beam. While spontaneous emission produces photons with exactly the energy

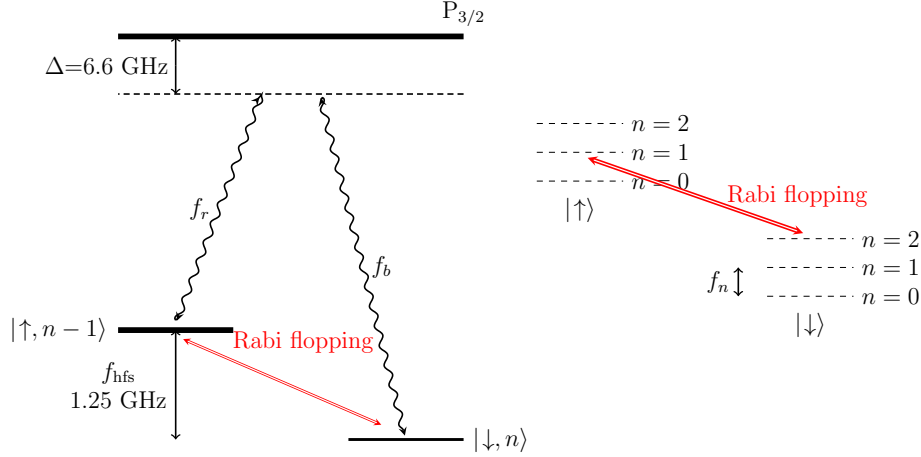


Figure 1.2: Left: Stimulated Raman transitions between $|\uparrow\rangle$ and $|\downarrow\rangle$ through a transient excited state detuned by 6.6 GHz from the actual excited state. Two laser beams are required for this operation: the Red Raman beam with frequency f_r and the Blue Raman beam with frequency f_b . Right: The first three vibrational states of $|\uparrow\rangle$ and $|\downarrow\rangle$. The Raman transitions result in the coherent coupling between $|\uparrow, n-1\rangle$ and $|\downarrow, n\rangle$. Note that adjacent vibrational states differ by f_n in angular frequency. Both figure are not drawn to scale.

difference between the excited state and the ground state, stimulated emissions in Raman transitions allow control of the energy and direction of the emitted photon. Since the linewidth of a $P_{3/2}$ hyperfine state is 19.4 MHz, a large detuning such as 6.6 GHz significantly suppresses spontaneous emissions, effectively reducing the transition to only between the two states of interest.

In order to couple $|\downarrow, n\rangle$ and $|\uparrow, n-1\rangle$, the frequency difference of the two Raman beams has to correspond to the energy difference between these two states. Given the hyperfine splitting between these two states (f_{hfs}), which can be controlled by adjusting the strength of the magnetic field, and the frequency difference between two adjacent vibrational states (f_n), the required frequency difference between the two lasers should be $f_{\text{hfs}} - f_n$. These two laser beams cause the population distribution

of ${}^9\text{Be}^+$ to oscillate between $|\downarrow, n\rangle$ and $|\uparrow, n-1\rangle$ with a frequency known as the Rabi frequency. A similar phenomenon is observed in nuclear magnetic resonance, where an oscillating magnetic field causes the nuclear magnetic moment to oscillate between two spin states.

With π -pulses, Rabi flopping leaves the atoms in the $|\uparrow\rangle$ state. We need a way to switch the atoms back to $|\downarrow\rangle$ while preserving its lower vibrational state, and a repump laser is used for this purpose.

1.4.2 Laser Repumping

To transfer $|\uparrow, n-1\rangle$ to $|\downarrow, n-1\rangle$, we use a σ^+ polarized laser beam to excite the atoms to a state in $P_{3/2}$ with $m_F = 2$. Due to the large hyperfine splitting (1.25 GHz) in the ground state, this laser is resonant with $|\uparrow\rangle$ while largely detuned from $|\downarrow\rangle$. From the excited states, angular momentum selection rules allow the atoms to decay to one of the three ground states: $|2, 2\rangle$, $|2, 1\rangle$, or $|1, 1\rangle$.⁵ In the first case, we have successfully arrived at $|\downarrow, n-1\rangle$. In the second case, we apply an rf drive at a frequency of f_{hfs} to pump the atoms back to $|\uparrow\rangle$. The atoms from the last case, along with those pumped by the rf drive to $|\uparrow\rangle$, will be resonant with the repump laser beam again. Through repeated Raman transitions and repumping, all of the atoms are eventually transferred to $|\downarrow, 0\rangle$, where they are no longer coupled with $|\uparrow\rangle$ because there is no $|n = -1\rangle$ vibrational level.

⁵The selection rule is $\Delta m_F = \pm 1, 0$, but there is no $|2, 3\rangle$ or $|1, 3\rangle$ states.

1.5 An Overview

We have introduced all of the required laser beams for state initialization, detection, and cooling of the logic ion. Fig 1.3 lists all six required laser beams with specific frequencies and polarizations attached. Through injection current modulation of the external cavity diode laser (ECDL), we obtain an optical sideband detuned by Δ (~ 6.6 GHz) from the carrier frequency (f_L).⁶ The detection, cooling, detuned cooling, and repump beams can be obtained from modulating the optical sideband using acousto-optic modulators (AOMs). The carrier is also modulated by AOMs to generate the Red Raman and the Blue Raman beams. Note that with δ at around 600 MHz, the detuned cooling beam can address all of the hyperfine levels in the ground state. The polarization choices of the first four σ^+ polarized lasers listed in the figure are required for angular momentum conservation, as discussed earlier in this chapter. Because non-resonant laser fields cause Stark shifts in $|\downarrow\rangle$ and $|\uparrow\rangle$, both Red Raman and Blue Raman beams contain σ^+ and σ^- in order to minimize the energy shift.[5] In addition, the Blue Raman has π polarized light so that along with the σ^- light in Blue Raman, we obtain the desired Raman transitions.

My thesis helps to build such a laser system as specified in Fig. 1.3. In Chapter 2, I present a laser locking system that I built to stabilize the frequencies of these lasers. In Chapter 3, I provide the details of using injection current modulation to produce the detuning (Δ) from the excited states.

⁶The figure shows $\Delta \sim 9$ GHz, that was our original plan. As we discovered in Chapter 3, our ECDL can only be modulated up to 6.6 GHz. This detuning should still be large enough.

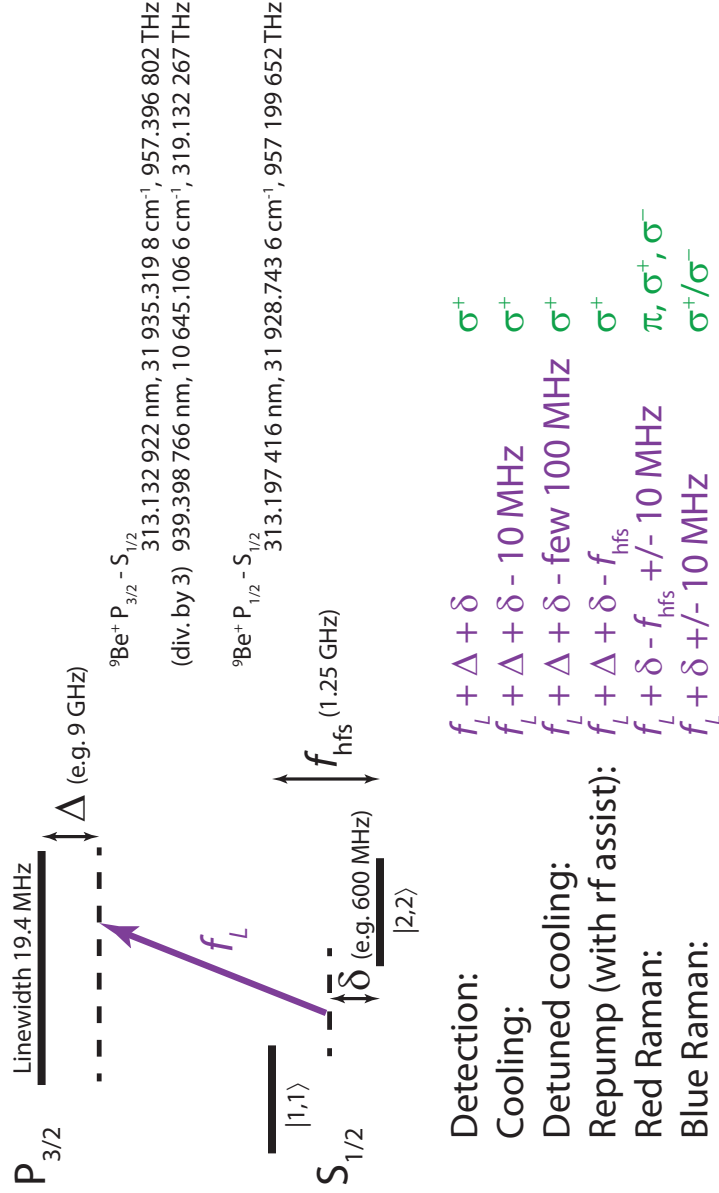


Figure 1.3: The laser beams needed for cooling and state initialization of ${}^9\text{Be}^+$. f_L refers to the carrier frequency of the external cavity diode laser; δ and the specified frequencies detunings in MHz are realized using the acousto-optic modulators and Δ results from injection current modulation. Figure courtesy of Professor Hanneke.

Chapter 2

Frequency Stabilization: The Scanning Fabry-Perot Cavity

A stable lasing source is integral to an effective quantum logic spectroscopy setup. More specifically, efficient state preparation and cooling of the logic ion, ${}^9\text{Be}^+$, requires that our lasers are stable enough for the linewidth of a $P_{3/2}$ excited state, which is 19.4 MHz (refer to Chapter 1 for detail).

In this chapter, we present a laser locking system that uses a confocal Fabry-Perot cavity to transfer the frequency stability of a helium-neon laser to our tunable lasing source, the external cavity diode laser (ECDL). The F-P cavity detects laser frequency drifts by comparing the wavelengths between the ECDL and the HeNe laser using a common length reference between two spherical mirrors. In order to obtain sensitive detection, which is critical for effective frequency stabilization, the common length reference must be kept stable. This concern guides the construction of the cavity as we took measures to stabilize the temperature and pressure within the cavity.

2.1 System Setup

A laser becomes resonant with the Fabry-Perot (F-P) cavity when an integer multiple of the laser's wavelength fits into its beam path within the cavity. At resonant conditions, we observe transmission peaks at the outputs of the F-P cavity. As we continuously scan the cavity length at a constant speed, a stable laser registers transmission peaks at equal time intervals. When the frequency drifts, this time interval varies. This allows a scanning F-P cavity to translate frequency drifts into transmission peak drifts when observed on an oscilloscope.

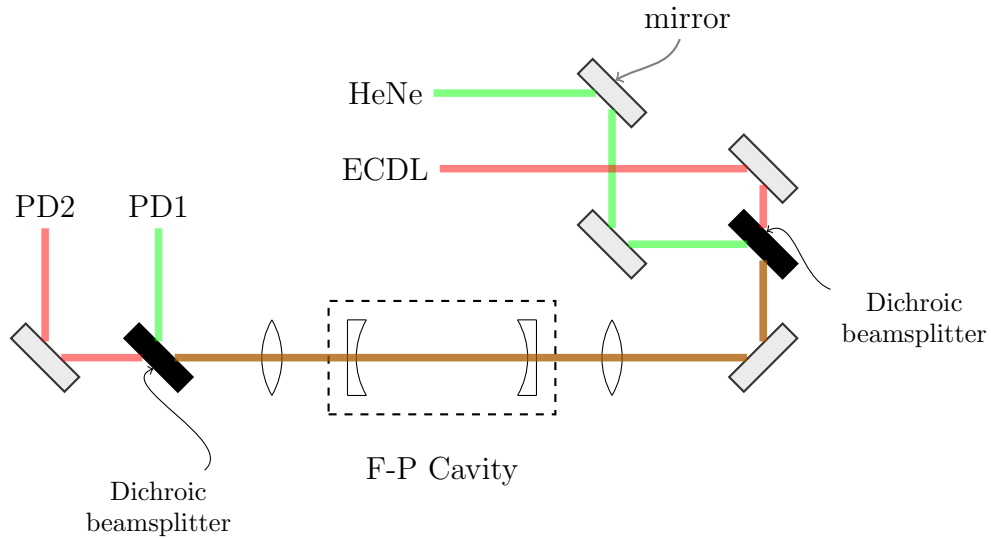


Figure 2.1: F-P cavity setup. The HeNe and IR beams are combined to a dichroic beamsplitter, where the HeNe beam is reflected and the IR is transmitted. The combined beam passes through the F-P cavity, until another dichroic beamsplitter splits them up on the other end of the cavity. Each beam is then detected by a photodetector. Note that some auxiliary mirrors used in practice to help direct beams are omitted in this figure.

We use a helium-neon laser (HeNe)¹ as a stable frequency reference. By measuring

¹We use an ultra stable Melles Griot HeNe (Part number 05-STP-901). Its stability in frequency-

the change in the time interval between an ECDL transmission peak and a HeNe transmission peak, we generate an error signal proportional to the laser frequency drift.

As shown in Fig. 2.1, the HeNe and the IR beam from the ECDL are combined onto the same beam path using a dichroic beamsplitter (Semrock FF678-Di01); the HeNe is reflected while the IR is transmitted. The converging lenses on both sides of the cavity enhance output signal by counteracting the diverging effects of the end mirrors.² At the output of the F-P cavity, the HeNe beam is separated from the IR using another dichroic beamsplitter.³ The transmission peaks of individual lasers are independently detected by photodetectors.

Fig. 2.2 illustrates how we implement the laser lock. As shown, the locking scheme is facilitated by a data acquisition device (NI DAQ, part number USB-6343), which is controlled by a Labview program.⁴ We obtain a triangle wave signal from the DAQ, which is amplified by a piezo driver before sending to the piezo in the F-P cavity. The cavity length is scanned as this piezo (Noliac NAC2123-A01) expands or contracts depending on the supplied voltage. The resulting transmission signals are detected by photodetectors and sent to the computer through the DAQ. By detecting changes in the spacing between a HeNe transmission peak and an IR transmission peak, the Labview program calculates a corresponding correction based on a proportional-integral-derivative (PID) algorithm. Since the ECDL frequency can be tuned by

stabilized mode is specified at 3 MHz over 8 hours.

²Our end mirrors are plano-concave, as demonstrated in Fig. 2.1. Without the converging lens, laser light incident on an end mirror will diverge within the cavity, causing the beam path to stray too far from the central axis and resulting in poor output signal.

³We divide one Semrock beamsplitter into two independent beamsplitters.

⁴The program is titled JeffLock; it is inherited from the DeMille lab at Yale. It is the only Labview program needed to automatically lock the laser frequency to the HeNe.

tilting the diffraction grating (see Sec 2.3.1 for detail), the DAQ sends a correction voltage to another piezo driver, which controls the piezo behind the diffraction grating to correct for frequency drifts.

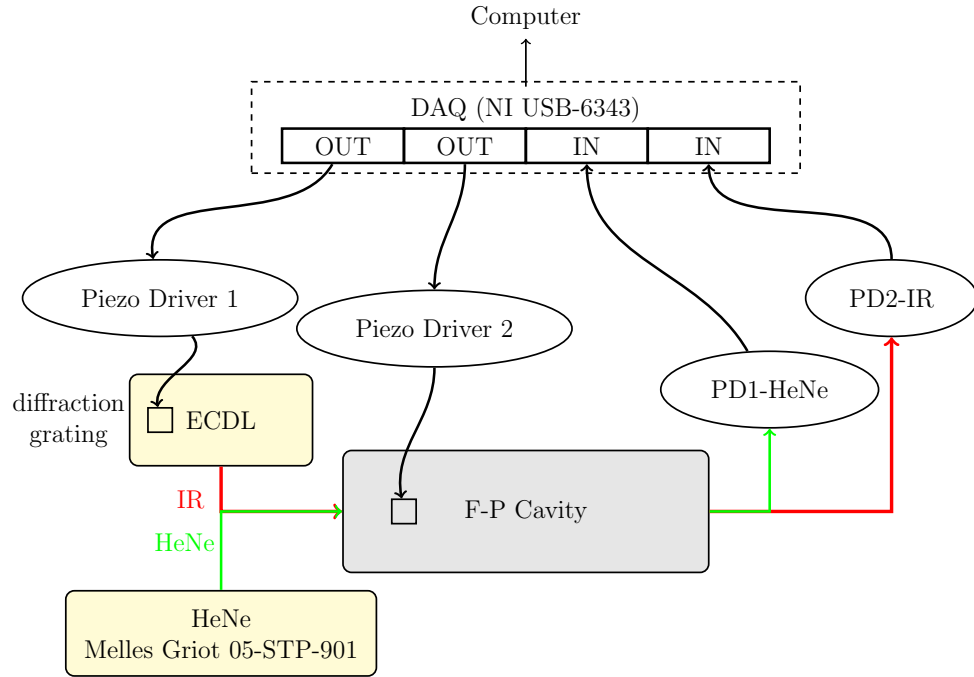


Figure 2.2: An illustration of the analog inputs and outputs of the data acquisition device (DAQ). The DAQ controls the piezos in the F-P cavity in the ECDL. It also reads HeNe and IR outputs from the photodetectors.

2.2 The Confocal Fabry-Perot Cavity

In the previous section, we see the central role of the Fabry-Perot (F-P) cavity in our locking scheme. We now introduce the confocal model that we adopted in our lab and describe its properties.

2.2.1 The Basic Theory

An F-P cavity consists of two end mirrors whose highly reflective surfaces face each other. A beam of light entering the cavity will make multiple passes between the mirrors. When these beams interfere constructively, the intensity of light builds up dramatically. Under this resonant condition, the high laser intensity within the cavity leads to transmission despite low transmittance of the end mirrors.⁵

In a confocal F-P cavity, the foci of two concave spherical mirrors coincide at the center of the cavity. This requires that the two end mirrors have equal radius of curvature (R) and that their separating distance (L) is equal to R . As will be seen, the confocal design is convenient because its behavior is largely insensitive to the shape and position of the input beam.

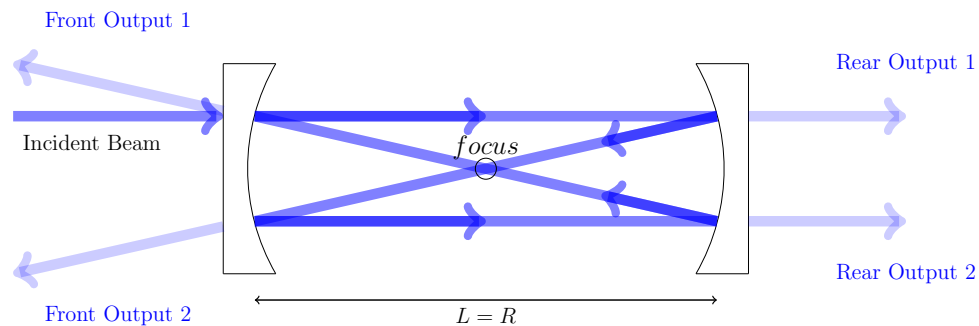


Figure 2.3: The beam path of a parallel beam incident on the F-P cavity. Arrows indicate propagation directions. The focal point is located at the center of the cavity, where the beam paths intersect. The distance between the mirrors corresponds to the radius of curvature (R). This figure is not drawn to scale.

In Fig. 2.3, the incident beam travels a distance close to $4L$ within the cavity before retracing its path. At resonance, there are two output beams at each side of

⁵High reflectivity of the end mirrors necessarily corresponds to low transmittance. Since the resonant effect is more important, higher reflectivity is usually better.

the cavity. While the front outputs diverge, the rear outputs propagate in the same direction as the incident beam. In principle all four outputs observe transmission peaks. In practice we choose one of the rear outputs as our signal because of the relatively small beam size.

Note that the incident beam does not have to be propagating along the central axis of the cavity. Any incident beam parallel to the central axis will have a beam path similar to the one described in Fig. 2.3. This makes the confocal cavity insensitive to beam positioning, which avoids many complications.

As we vary the cavity length L , constructive interference occurs when there is an integer number of wavelengths in the beam path. At constructive interference, the laser intensity is greatly amplified due to the highly reflective mirrors. This results in transmission peaks at the outputs of the F-P cavity whenever the following condition is satisfied:

$$n\lambda = 4L, \tag{2.1}$$

where n is the integer mode number and λ is the wavelength of the incident beam.

According to Eq. 2.1, changing L by $\lambda/4$ maintains the cavity at resonance. Therefore, adjacent transmission peaks differ in L by $\lambda/4$. This distance is also called the Free Spectral Range(FSR) of the cavity.

The FSR is more conventionally expressed in terms of frequency. Recall that wavelength and frequency are related by the speed of light. The frequency difference between two adjacent transmission peaks is

$$\text{FSR} = \frac{c(n+1)}{4L} - \frac{cn}{4L} = \frac{c}{4L}, \tag{2.2}$$

where c is the speed of light in vacuum.⁶ Since the radius of curvature for the mirrors is 100mm, the cavity length at confocal condition is also 100mm. This corresponds to an FSR of 750 MHz.⁷

Another important parameter for F-P cavities is the finesse(f). It relates the full width at half maximum(FWHM) of the transmission peaks to the FSR:

$$f = \frac{\text{FSR}}{\text{FWHM}}. \quad (2.3)$$

Since the finesse is related to the energy stored in the resonant cavity, it is determined by the reflectivity (r) of the cavity mirrors[6, p 119]:

$$f = \frac{\pi\sqrt{r}}{1-r}. \quad (2.4)$$

For our mirrors, $r = 97(1)\%$,⁸ leading to a calculated finesse of 103(35). Hence we expect the FWHM of our transmission peaks to be around 7(3) MHz. For logistical reasons, we used a different confocal F-P cavity for injection current modulation in Chapter 3. For that F-P cavity, the FSR is 500 MHz and the finesse is > 1569 . Because of the extremely high finesse, the observed transmission peaks during injection current modulation are much narrower.

The above discussion offers an intuitive way to think about the confocal F-P cavity.

⁶In reality, our cavity is not in vacuum. The speed of light in the cavity is slightly less than c . Since what we want is a stable beam path in between the mirrors, we take measures to stabilize the temperature and pressure within the cavity to keep the index of refraction of the air stable.

⁷The FSR is technically not a constant—it changes by ≈ 1 kHz for adjacent modes. By fitting a transmission peak to the Lorentzian distribution, the uncertainty of the peak position is on the order of a few hundred kHz. Since we are only scanning over a few modes, the FSR is effectively constant for our purposes.

⁸Note that this is the reflectivity of laser power, not the electric field.

In reality, the mode number n in Eq. 2.1 includes both the axial and transverse mode numbers. The axial modes represent the standing waves between the two cavity mirrors. The transverse modes are manifested in the electric field distribution of the beam's profiles perpendicular to the direction of propagation. These field distributions can be described by a combination of the Gaussian distribution and the Laguerre polynomials. The fundamental transverse mode is just a Gaussian beam profile; laser outputs are typically in this mode.

Taking both kinds of resonant modes into consideration, the resonant condition in terms of frequency is actually [7]

$$\nu = \frac{c}{2L} \left[m + \frac{1}{\pi} (1 + l + p) \cos^{-1} \left(1 - \frac{L}{R} \right) \right], \quad (2.5)$$

where m is the axial mode number, l and p represent the angular and radial mode number for the transverse modes. Since cavity resonance depends on transverse modes as well, it becomes necessary to match the beam size and divergence of the incident beam with those of the cavity. This practice is called mode-matching.

Fortunately, for confocal cavities, $L/R = 1$ and $\cos^{-1}(1 - L/R) = \pi/2$. Eq. 2.5 simplifies into

$$\nu = \frac{c}{4L} [2m + 1 + l + p]. \quad (2.6)$$

If $l + p$ is odd, $\nu = nc/2L$, where n is an integer. On the other hand, if $l + p$ is even, $\nu = nc/2L + c/4L$. The even transverse modes have resonant frequencies exactly halfway between the odd transverse modes. This is why our FSR is effectively $c/4L$ as mentioned in Eq. 2.2 and the transverse modes are degenerate within the cavity. This significantly simplifies laboratory procedures because there is no need to shape

the beams to match the transverse modes within the cavity.

2.2.2 Athermal Cavity Design

A functional cavity requires some essential features. First, the cavity mirrors have to be aligned and secured in place. The distance between the two mirrors has to be adjustable in order to achieve the confocal condition. As we introduced in Sec. 2.1, the cavity also needs a piezo that scans the cavity length over a few transmission peaks.⁹ Secondly, as part of a stabilizing scheme, it is important to keep the system itself stable under usual lab temperature and pressure variations.

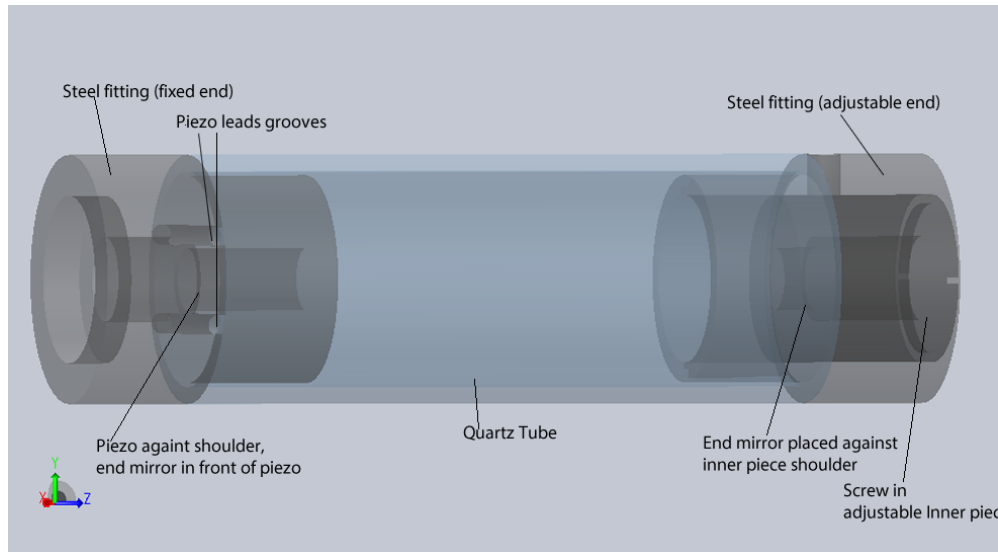


Figure 2.4: SolidWorks assembly of the actual cavity design.

With all these considerations in mind, we adapted a clever F-P cavity design from the Demille Group at Yale University. Fig. 2.4 shows a 3-D model of the actual

⁹Recall that the FSR is equal to $\lambda/4$ for confocal F-P cavities. If we want to observe 10 transmission peaks, we only need to vary the cavity length by around $2\mu\text{m}$.

design. The cavity has two steel fittings glued to each end of a quartz tube. Each steel fitting contains a through-hole that allows laser input and output. At the fixed end, a ring-shaped piezoelectric transducer is sandwiched between a flat-surfaced shoulder around the through-hole and a cavity mirror. At the adjustable end, the outer steel fitting contains a screw-in inner piece; the other cavity mirror directly rests on the flat-surfaced shoulder around the through-hole in the inner piece. This mobile inner piece allows us to adjust the distance between the two cavity mirrors manually. Both cavity mirrors are secured in place by tightening the retaining rings on the o-rings behind the mirrors. The two piezo leads are channeled through the grooves as shown in Fig. 2.4. Note that the shoulder at the fixed end is carefully aligned with the rim of the quartz tube to within a few thousandths of an inch; this is a crucial feature for the athermal design as we will come to explain soon.

This design is both realistic to build and user-friendly. As the assembly in Fig. 2.4 shows, there are very few components. Moreover, there are only two components that require high machining precision. The first is the alignment between the shoulder at the fixed end and the quartz rim as described in the previous paragraph. The second is the length of the quartz tube. As for user-friendliness, the mobile inner piece allows manual adjustments of the cavity length while the piezo at the fixed end implements finer adjustments for transmission peak observations.

Apart from these beneficial features, the design also maintains a stable cavity length under small temperature drifts. To see how this feature is made possible, we begin by determining the cavity length from the dimensions of the cavity components. Closely examining Fig. 2.4, the cavity length can be calculated from the following dimensions:

1. The length of the quartz tube (q). It fixes the distance between the two steel fittings.

2. The distance between the cavity mirror and the rim of the quartz tube at the adjustable end. We refer to this distance as x . In our case, the inner piece extends into the quartz tube so that the mirror is entirely contained within the tube. This is why the cavity length is shorter than q , hence we subtract x from q when calculating the cavity length.

3. The thickness of the piezo actuator (p). At the fixed end, the mirror is stacked on top of the piezo, which means p constitutes part of the cavity length.

4. The curvature length (y) of the mirrors. This is the distance between the piezo and the concave surface of the spherical mirror. The geometrical detail is presented in Fig. 2.5.¹⁰ We do not need to consider y for the mirror at the adjustable end because that distance is part of q .¹¹

For an athermal F-P cavity, the cavity length remains constant under small temperature fluctuations. In terms of the variables introduced in the list, the cavity length is just $q - x + p + y$. Under a temperature change, the relevant components expand or contract individually, yet the total change in cavity length remains unchanged if

$$\alpha_{\text{quartz}}q - \alpha_{\text{steel}}x + \alpha_{\text{piezo}}p + \alpha_{\text{mirror}}y = 0, \quad (2.7)$$

where the α 's are the coefficients of thermal expansions for each material indicated

¹⁰In order to use y , which is the distance from the center of the mirror to the piezo, we are assuming that the beam paths are close to the central axis of the cavity. This is a reasonable approximation since the mirrors are small (mirror diameter is 12.7mm).

¹¹If we want to be really precise here, the mirrors have a slightly different coefficient of expansion from the quartz tube, so in principle we should also consider y at the adjustable end. However, since the coefficient of expansion for the cavity mirrors is $0.57 \times 10^{-6} \mu\text{m}/\text{m} \cdot ^\circ\text{C}$ at 20°C and it is $0.4 \times 10^{-6} \mu\text{m}/\text{m} \cdot ^\circ\text{C}$ at 20°C for the quartz tube, this approximation is close enough for our purposes.

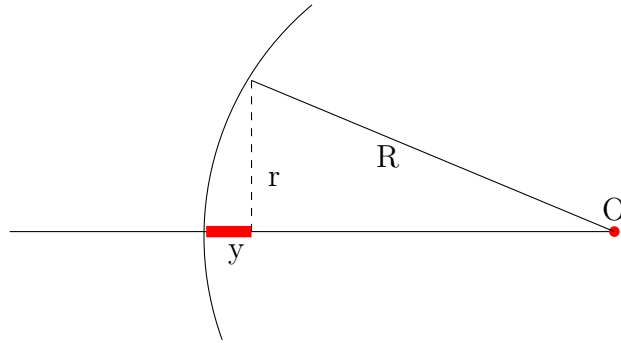


Figure 2.5: Geometry of a spherical mirror. R is the radius of curvature, r is the mirror radius, and y is the curvature length.

by the subscripts.

Since the piezo thickness, curvature length, and the coefficients of thermal expansions are given, we need to find a combination of q and x that satisfies Eq. 2.7. Furthermore, the confocal condition allows us to substitute $q + p + y - L$ for x . Using this constraint and Eq. 2.7, we obtain the required length for the quartz tube in order for our cavity to be athermal. Note that in practice, x automatically satisfies the constraint when we tune the cavity to confocal condition.

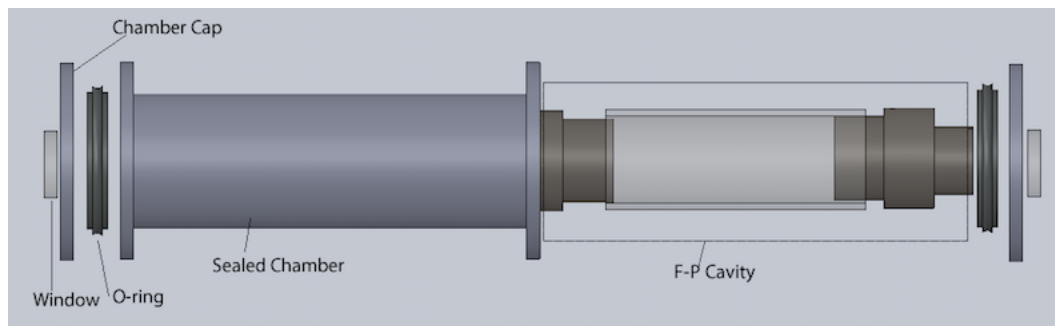


Figure 2.6: An exploded view of the sealed chamber containing the F-P cavity.

To further improve the stability of the F-P cavity, we acoustically isolate it by

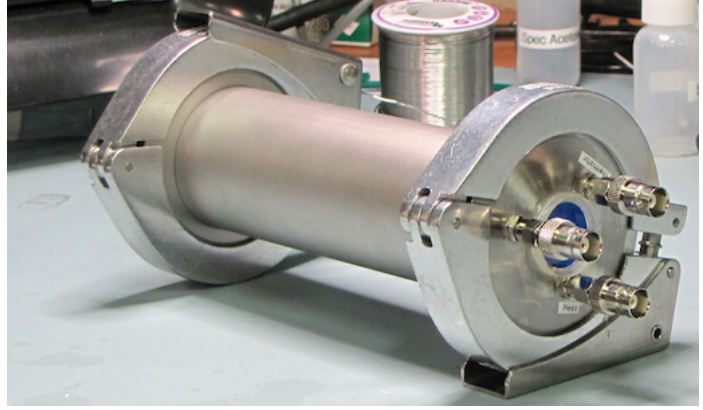
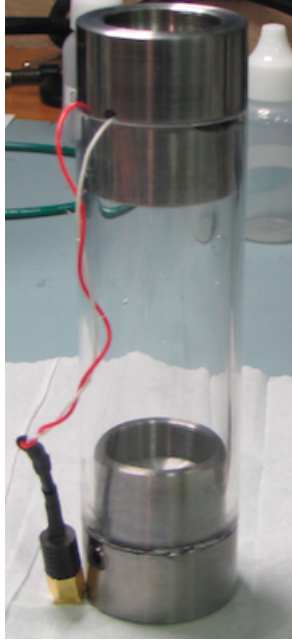


Figure 2.7: Left: a photo of the assembled F-P cavity. The piezo leads are soldered to an SMA connector for convenience. Right: a photo of the cavity enclosed in the chamber.

wrapping it in a piece of styrofoam-cushioned lead sheet and enclose it in a sealed chamber to keep the pressure constant within the cavity. A thermistor (Thorlabs TH10K) is placed next to the steel fitting at the fixed end to monitor the temperature within the chamber when needed. Fig. 2.6 shows an exploded view of the SolidWorks drawing for the whole assembly; a photo of the F-P cavity and the sealed chamber are also attached in Fig. 2.7.

The complete laser lock setup is mounted on a 1'×2' breadboard, as shown in Fig. 2.8. This mobile board contains both the HeNe tube and the F-P cavity, along with the beamsplitters, mirrors, and photodetectors. The laser beam to be stabilized is introduced into the system by mounting the optical fiber on a fiber mount situated between the HeNe tube and the F-P cavity. By fixing the fiber mount in place, there

is no need for realignments when switching to a different laser. All of these features make our laser lock a compact, convenient, and versatile system.

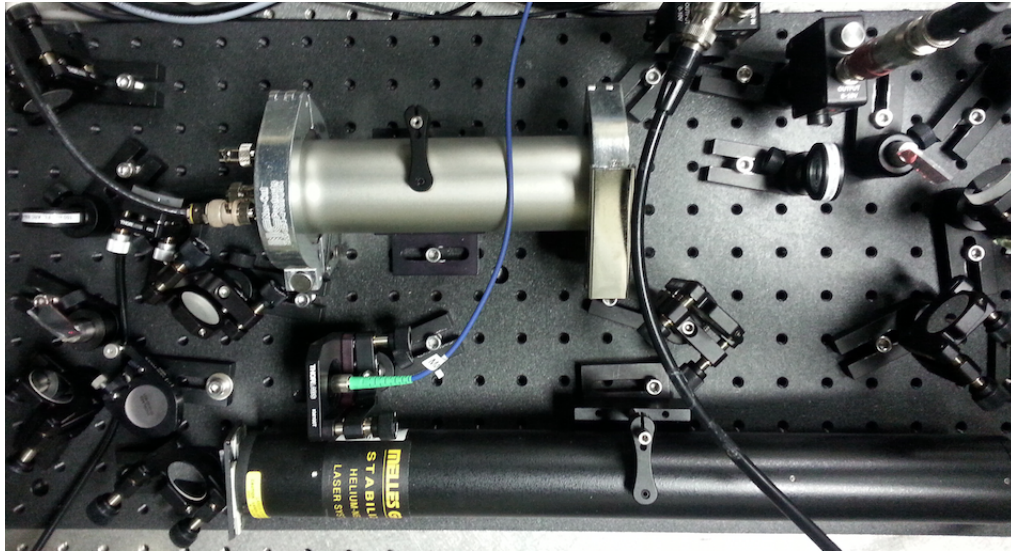


Figure 2.8: The completed setup on a mobile breadboard.

2.2.3 Obtaining the Confocal Condition

Before we wrap up the F-P cavity in a pressure chamber, we need to first adjust the cavity length to confocal condition. The cavity length can be adjusted by manually changing the position of the inner piece. The tuning procedure relies on two key features that distinguish resonant peaks at confocal condition: the symmetry of the transmission peaks and the dramatic increase in output intensity.

The symmetry in the transmission peaks is related to the transverse mode-degeneracy of the confocal F-P cavity. When the transverse waves are non-degenerate, the output intensity of the transmission peaks is distributed over many non-axial peaks, causing the transmission peaks to be asymmetric. The dramatic increase in output intensity

is due to the mode degeneracy of confocal cavities. While the input beams have to be mode-matched for non-confocal cavities, the confocal cavity is not as sensitive to beam alignments and beam sizes.

Fig. 2.9 shows a transmission peak of the HeNe at confocal condition. The peak is fitted to a Lorentzian distribution:

$$f = y_0 + \frac{a}{1 + \left(\frac{x-x_0}{b}\right)^2}, \quad (2.8)$$

where the peak height is conveniently a and the full width at half maximum (FWHM)

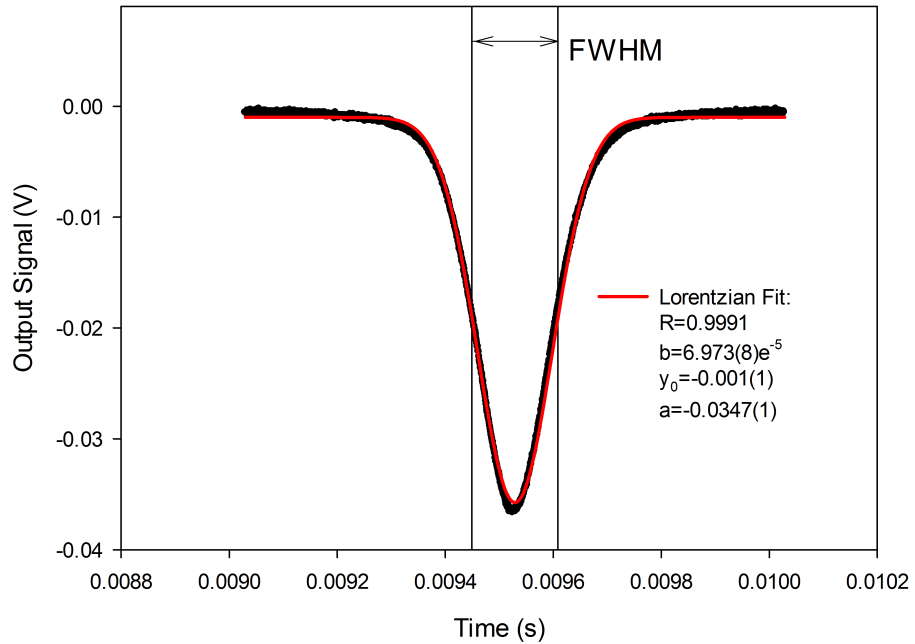


Figure 2.9: A HeNe transmission peak fitted to a Lorentzian. Fit parameters from the regression are attached, where R is the coefficient of correlations for the fitted line and the rest are explained in Eq. 2.8.

is $2b$. The fitted parameters are attached to the figure. The coefficient of correlations (R) is very close to 1, indicating a close fit of the resonant peak to the Lorentzian distribution. Using the time interval between two transmission peaks and the fact that our confocal cavity FSR is 750 MHz, we calculate the FWHM of the transmission peak in Fig. 2.9 to be 18(9) MHz. This is consistent with theoretical prediction of 7(3) MHz from the cavity finesse.

The large uncertainty for the calculated FWHM is related to the irregularity in the time interval observed between two successive peaks. As the piezo drives over a full triangle wave, the nonlinear behavior is evident in Fig. 2.10. In fact, the width of the peaks generally narrows as the piezo voltage increases as well. These observations imply that the piezo is more responsive to higher voltages.

The non-linear piezo response does not really affect system performance because we are only scanning over 2 transmission peaks and the piezo response is locally quite linear. More importantly, frequency lock relies on keeping the distance between a diode laser transmission peak and a HeNe transmission peak constant. Although the error signal might not linearly reflect frequency drifts, the system should still be able to detect error signals and lock the laser. However, non-linear piezo response does complicate inferring precise frequency drifts from changes in peak locations.

2.3 The External Cavity Diode Laser

ECDL's are versatile because of their narrow linewidth, tunability, single-mode output, and often times ease of construction. [8] However, precisely because it is tunable, the ECDL is not locked to an atomic transition thus requires an external laser

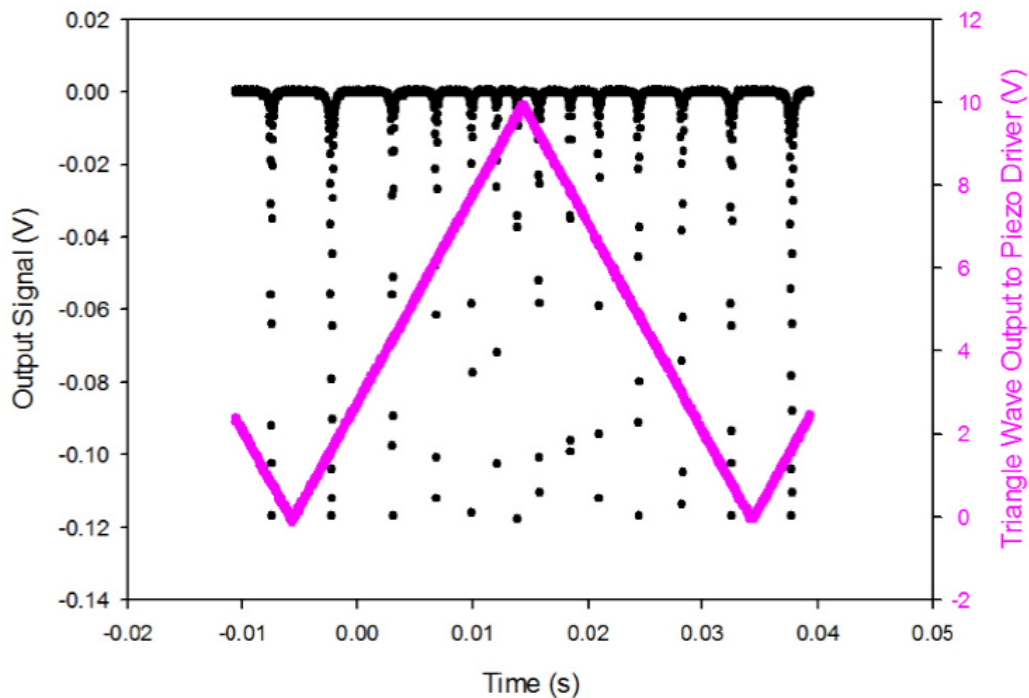


Figure 2.10: HeNe transmission peaks obtained from scanning the cavity length with a triangle wave. Note that they get closer at higher piezo voltages, indicating a faster piezo displacement there.

lock such as the one we are building. The major components of an ECDL are a laser diode and a diffraction grating. The laser diode contains its own optical cavity between its two crystal facets (refer to Chapter 3 for more details). Like the F-P cavity, the laser diode lases at frequencies corresponding to constructive interferences within its optical cavity, leading to a broad emission spectrum. The diffraction grating selects a very narrow range of these emitted frequencies as the output of the ECDL.

The “external cavity” refers to the optical cavity formed between the rear crystal facet of the laser diode and the diffraction grating. Fig. 2.11 is a photo of our ECDL,

where I have labeled the beam path. The frequencies that the diffraction grating selects will be reflected by a mirror fixed at an angle with the diffraction grating. Note that the mirror co-tilts with the diffraction grating such that the output beam path drifts minimally during frequency tuning.

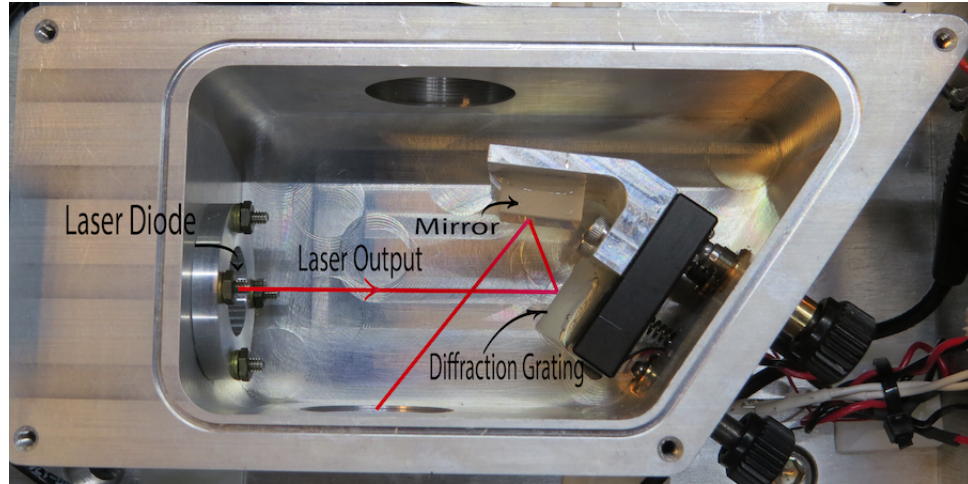


Figure 2.11: A photo of our external cavity diode laser. Relevant parts are labeled and the beam path is illustrated.

As with the F-P cavity, we can determine the free spectral range of the external cavity by noting the beam path of the laser within the cavity. In this case, the beam path is twice the cavity length because the beam only makes one round trip before repeating its original path. The expression for the FSR is therefore

$$\text{FSR} = \frac{c}{2L_{\text{eff}}}, \quad (2.9)$$

where c is the speed of light, and L_{eff} is the effective cavity length. According to our measurement of the cavity length, the FSR is estimated to be around 2.4 GHz. It is hard to determine the effective cavity length because as mentioned earlier, the laser

diode also has its own optical cavity. This estimate is therefore revised in Sec. 3.3.2 to ~ 2.2 GHz.

Since temperature drifts affect ECDL frequency stability, we monitor its temperature through a thermistor inserted into the steel case of the ECDL. We control the temperature of the ECDL using a thermoelectric module driven by Thorlabs TED200C.

2.3.1 The Diffraction Grating

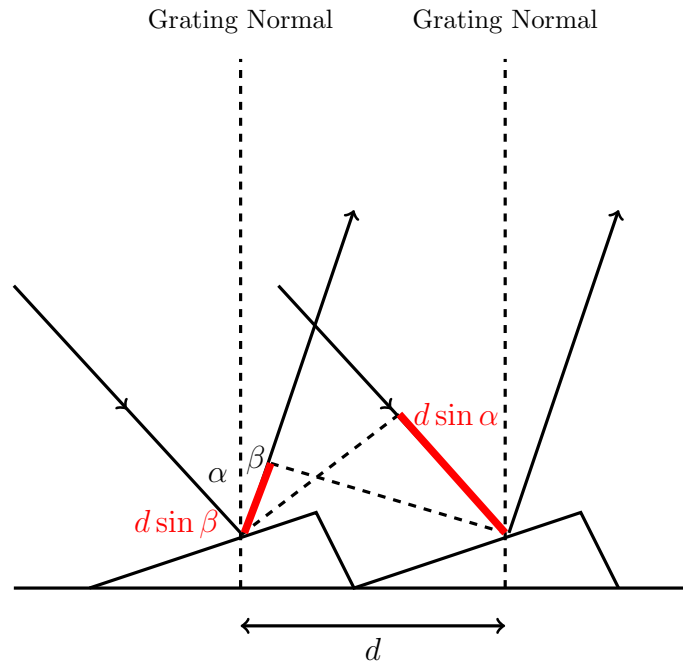


Figure 2.12: Illustration of rays incident on a blazed diffraction grating. The path differences are marked in red.

The diffraction grating contributes to the tunability and the narrow linewidth of the ECDL. Since both of these qualities are essential to our laser system, it is

worthwhile to discuss the mechanism behind this frequency selection.

Light incident on a diffraction grating will be diffracted into a series of interference patterns. Consider the geometry in the Fig. 2.12, where we show two grooves on the surface of a blazed diffraction grating. The diffracted rays from adjacent grooves (separated by d) interfere constructively when the total path difference between the two rays shown in the figure is an integer multiple of the incident wavelength (λ), or

$$d(\sin \alpha - \sin \beta) = m\lambda, \quad (2.10)$$

where α and β represent the incident and diffracted angle with respect to the grating normal and m is the integer diffraction order number.

If the diffracted light traces back to its incident direction, or $\alpha = -\beta$, it is in Littrow grating condition:

$$2d \sin \alpha = m\lambda. \quad (2.11)$$

The feedback from the optical cavity formed between the rear crystal facet of the diode and the diffraction grating enhances stimulated emission at the Littrow wavelength. According to Eq. 2.11, changing the angle of incidence determines the wavelength that satisfies the Littrow condition, which in turn determines the ECDL output.

In practice, we change the incident angle by tilting the grating normal. A piezoelectric transducer is placed behind the grating mount to control the selection of desired laser outputs. We use a blazed diffraction grating (Thorlabs GR-13-1208) in our ECDL. With 1200 grooves per mm, the distance between adjacent grooves is around $0.8\mu m$. Considering the geometry of our diffraction mount, the diffraction grating will be tilted at angle of 34.3° with respect to the external cavity axis in order

to select the 940nm beam. My calculations suggest that varying the laser wavelength by 1FSR requires a piezo displacement of $\sim 30\text{nm}$. This translates to a voltage of around 2 volts for our Noliac piezo actuator (part number NAC2123-A01). In reality, the piezo is less responsive than specified and requires much higher voltage.

2.4 System Performance

We successfully locked our ECDL to the HeNe using the setup presented in Sec. 2.1. However, the actual frequency stability of the ECDL is determined by the stability of the HeNe, the F-P cavity, and the precisions of the detection and software. This means that we need a second frequency reference to assess the stability of the system while it locks a laser to the HeNe. The mobile setup mentioned earlier in Sec. 2.2.2 conveniently allows us to adapt the laser lock to another laser. For testing purposes, we use our system to stabilize the frequency of a laser (not our ECDL) that is resonant with a thallium fluoride molecular transition in Professor Hunter’s lab.¹² With this setup, the molecular transition serves as the second frequency reference.

2.4.1 System Stability

A laser beam excites the thallium fluoride molecules from the ground state to one of the excited states when its frequency corresponds to the energy difference between the two internal states. Immediately following the excitation, spontaneous emissions release photons that are counted with a photomultiplier. Since excitation is extremely sensitive to laser frequency, the number of emitted photons changes drastically for

¹²The TlF transitions we observe are between the excited states ($B^3\Pi_1(0)$) and the various vibrational levels of the ground state ($X^1\Sigma^+(\nu)$). [9]

small laser frequency drifts.

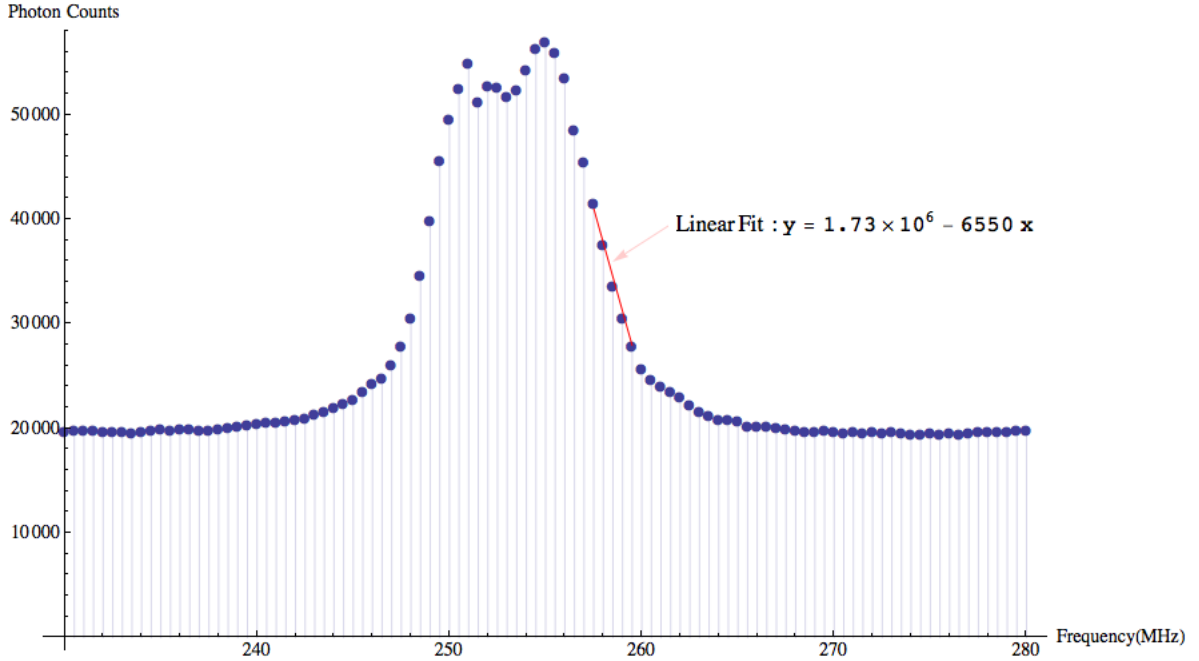


Figure 2.13: Thallium Fluoride Q70 vibrational level transition peak. Each point is an average of 20 consecutive photon counts at the same frequency. A weighted linear fit to the slope on the high-frequency side of the peak is marked in red.

In order to relate photon counts to the laser frequency, we vary the laser frequency at increments of 0.5 MHz while recording the corresponding photon counts. The result is a transmission peak as plotted in Fig. 2.13. Each data point in this figure is an average of 20 consecutive photon counts at the same laser frequency. The peak represents where the laser is most resonant. Fig. 2.13 shows that the linewidth of the TIF Q70 vibrational level transition is less than 10 MHz.

Since the photon counts are most sensitive to frequency changes at the slopes of the transition peak, we lock the laser in the region marked in red in Fig. 2.13. We fit the data in this region to a line, taking into consideration the standard deviations of

each averaged photon count. The resulting fit parameters are used to convert photon counts into frequency.

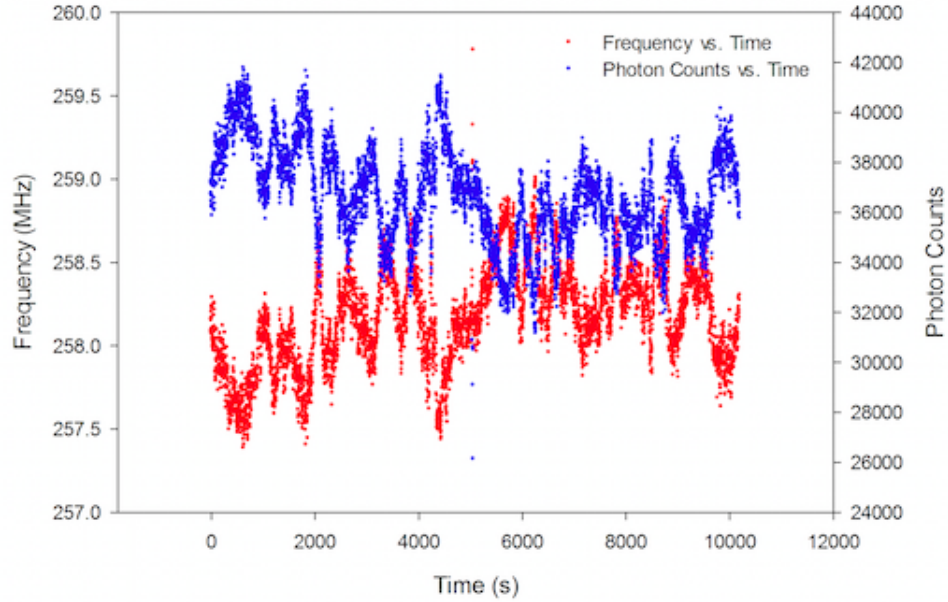


Figure 2.14: Frequency stability of the locked laser measured using the TIF molecular transition. The frequencies are converted from photon counts (also shown in this figure) using the linear fit parameters from Fig. 2.13

With the lock operating, variations in photon counts over a period of 3 hours are plotted in Fig. 2.14. Using the linear fit from the transition peak, we convert the photon counts into frequencies; the result is plotted in the same figure. Because we selected the declining slope where photon counts decrease with increasing frequency, the two plots in Fig. 2.14 are inverted. Note that throughout the 3 hours, frequency drifts are contained within a 2 MHz interval, which is better than the specified HeNe stability of the same amount for 1 hour.

The effectiveness of our laser lock is most apparent when we unlock the laser

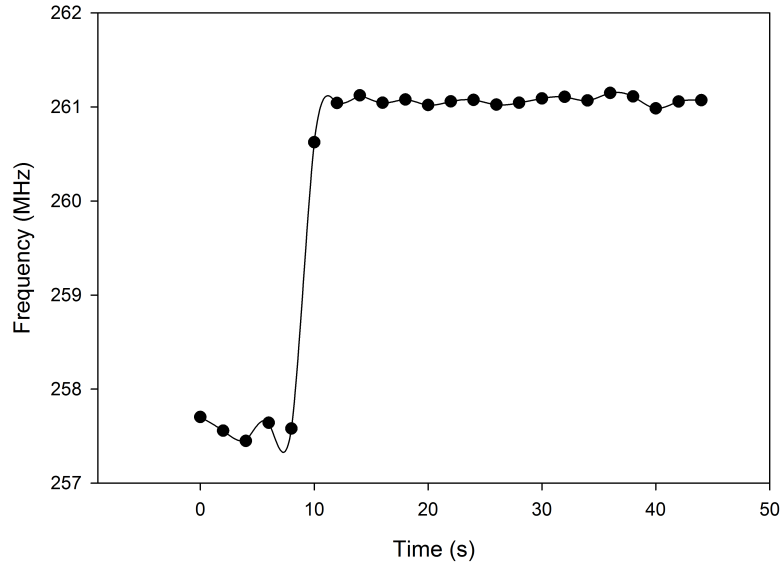


Figure 2.15: Laser frequency unlocked at the slope of the TlF Q70 transition peak.

frequency at the end of the 3 hour test. Fig. 2.15 shows that in a matter of seconds the frequency drifts off the transition peak. Note that the flat tail at the end merely represent background photon counts.

The Allan deviation plot is often used to show stability over different time scales. To obtain Fig. 2.16, we first partition the data shown in Fig. 2.14 into all possible bin sizes, which ranges from 2 seconds to about 1.5 hours. We then calculate the standard deviation for each bin size.¹³ Notice that I have boxed out a region where the Allan deviation declines before it become erratic. The decline shows that our locking scheme is effectively controlling frequency drifts at a time scale of about 10 minutes. The erratic oscillations at the end of the plot is due to the increasing bin size and decreasing number of bins used to calculate the standard deviations. The

¹³This calculation is explained in more detail in Appendix B.

Allan deviation plot shows that by using our locking system, the laser—and more importantly the system—is stable to within 200 kHz over 3 hours. Our system is performing exceedingly well!

2.4.2 Reaction to Temperature Drifts

When building the cavity, we emphasized the athermal design and the various features added to isolate the cavity from its surroundings. We now test the merits of these measures by observing how the system responds to temperature drifts.

We wrap a heater tape around the pressure chamber containing our F-P cavity. The thermistor within the pressure chamber reports a linear change of temperature at $0.003(1)^\circ\text{C}/\text{s}$. To keep this number in perspective, the normal temperature drift

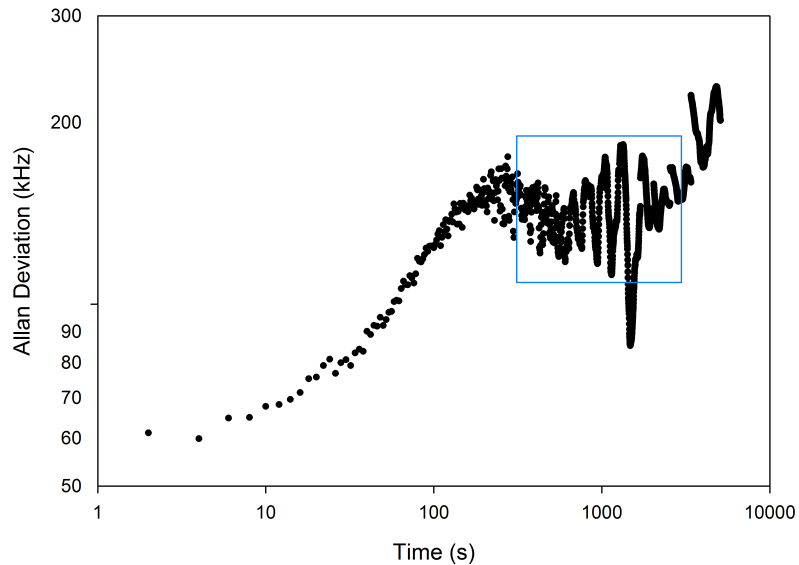


Figure 2.16: Allan deviation of laser frequency in log-log scale. The Allan deviation in the boxed region indicates long term stability.

within the cavity as reported by the same thermistor is only around a factor of 100 less than this.

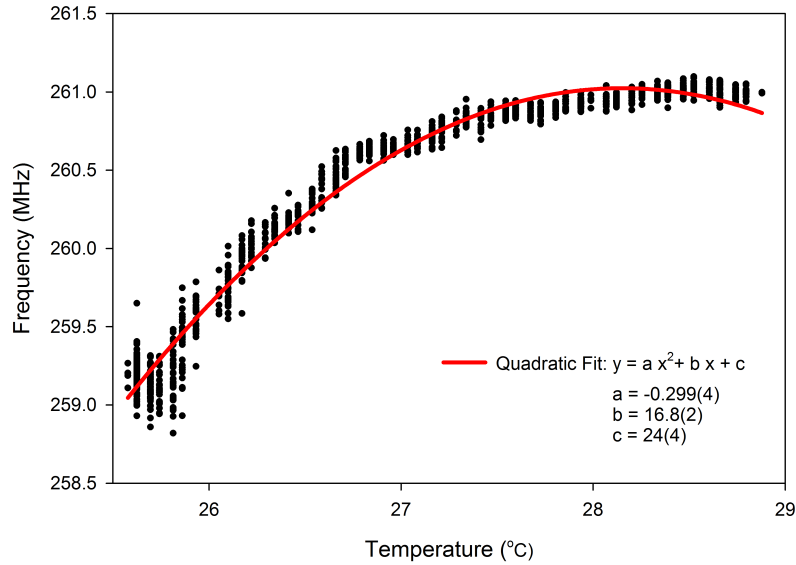


Figure 2.17: Frequency drift due to temperature change of the F-P cavity. Laser frequency is locked throughout. The plot is fitted to a quadratic curve with the parameters attached to the figure.

Fig. 2.17 shows the frequency drift under a consistent temperature change while the laser is locked. The system drifted over 1 MHz over 3°C. With a stability of around 200 kHz, a temperature drift of $\sim 0.6^\circ\text{C}$ will degrade the system. Since lab temperature rarely fluctuates this much, the laser lock is, as planned, “athermal” for small temperature variations.

The quadratic fit in Fig. 2.17 shows that the laser frequency seems to stabilize towards the end at higher temperatures. We are not sure about the reason behind this seemingly improving locking performance.

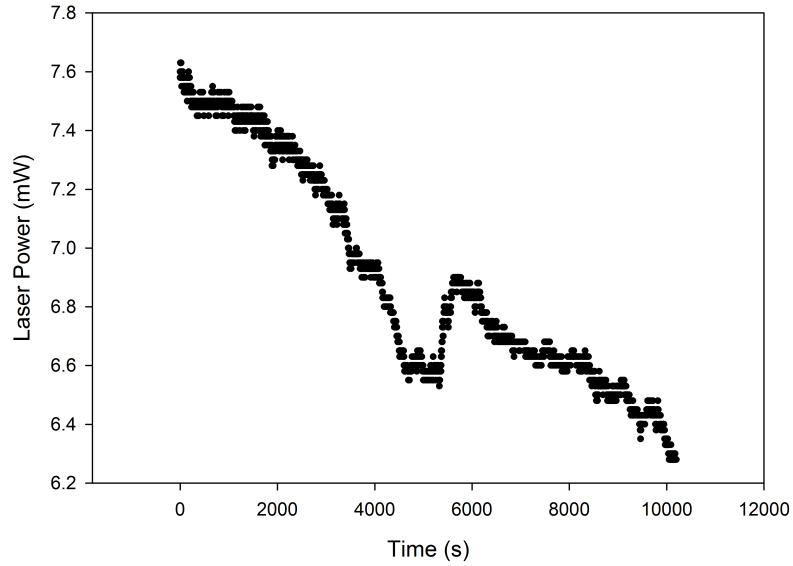


Figure 2.18: Laser power drift for the same time duration as Fig. 2.14.

2.4.3 The Other Factors

It is important to keep in mind that the detection of the emitted photons depend on other factors, most notably incident laser power. Variations in these factors contribute to the observed frequency drifts, which might exaggerate the actual frequency drifts. Fig. 2.18 shows the laser power drift as we took the data in Fig. 2.14. We observe a discontinuous change in laser power half way into the test. Since this fluctuation is mirrored in the observed photon counts, the laser power drift may contribute to the unusually noisy photon counts in this region.

So far we have been using photon counts observed by one of the detectors. There is another detector that also tracks the number of emitted photons from the same group of molecules. Since frequency drifts affect both detectors, photon counts from the two detectors should correlate to each other if there are no other factors influencing the

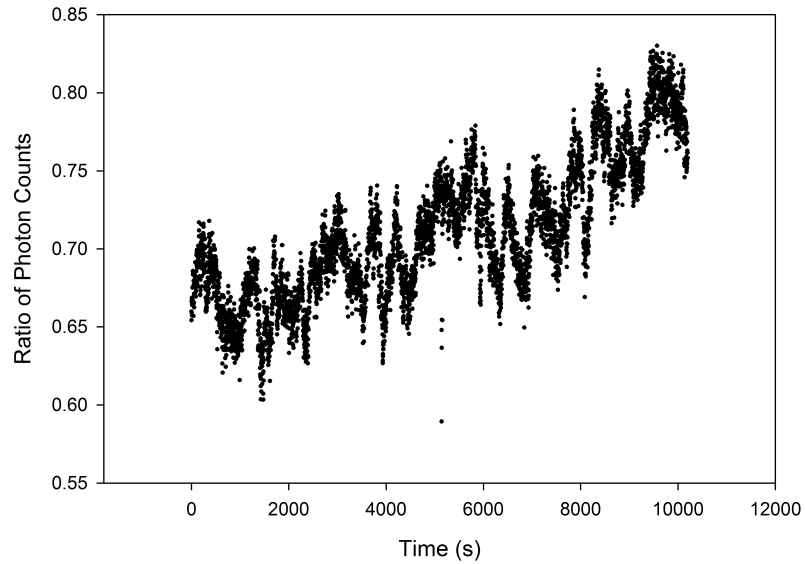


Figure 2.19: Ratio of photon counts obtained by Channel A and Channel B.

photon counts.

In Fig. 2.19, we plot of ratio of photon counts observed by the two detectors over time. The drift in the ratio demonstrates that there are other factors that influence the two detectors in different ways.

The F-P locking system has demonstrated its ability to effectively stabilize laser frequency by maintaining the long term laser stability at around 200 kHz. Moreover, the various factors that might influence photon detection implies that the system might actually perform even better than what we observed.

Chapter 3

Injection Current Modulation

Recall from Chapter 1 that efficient stimulated Raman transitions require a large detuning, Δ , from the excited state. This large detuning complicates the process of obtaining the six required laser beams from the stabilized ECDL laser. In this chapter, we discuss a convenient method that can potentially be an alternative to expensive electro-optical modulators (EOM's), which have been shown to work for a system similar to ours.[10]

Many groups have achieved frequency modulations above 7 GHz with more than 2% of the carrier power in the first sideband through direct microwave modulations of external cavity diode lasers. [11, 12] We followed a similar procedure and were able to modulate our ECDL up to 6.6 GHz with 3% of the carrier power in the first sideband. We also investigated the dependence of modulation response on a variety of factors; most of the observations confirm theoretical expectations. These observations can help us to choose appropriate conditions to obtain an optical sideband suitable for our experiments.

3.1 Experimental Setup

We implement injection current modulation using the setup illustrated in Fig. 3.1. The DC bias current is combined with an rf signal¹ through a bias T, and the superimposed signal is used to drive the laser diode. The modulated ECDL output is sent to a scanning Fabry-Perot cavity similar to the one we built.² We scan this F-P with a triangle wave to observe the carriers and sidebands.

We make no attempt to impedance-match the rf power, but we monitor the reflected power using a directional coupler. The crystal detector measures the reflected rf power, which can be used to gauge the actual rf power received by the laser diode.

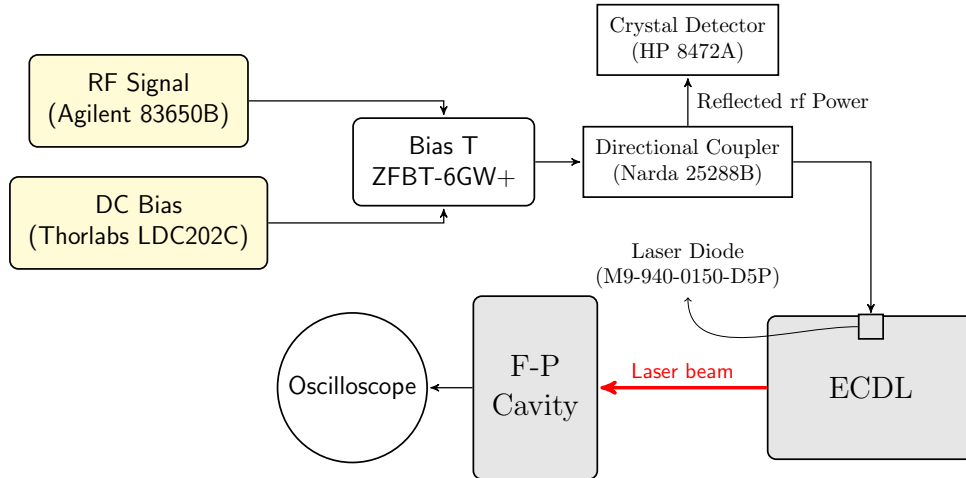


Figure 3.1: Experimental setup for injection current modulation. The rf signal is combined with the DC bias current through the bias T. The directional coupler picks up the reflected rf power, which is measured by the crystal detector. The modulated laser output is analyzed by a scanning F-P cavity. Part numbers are attached when applicable.

¹The rf signal generator is provided by the Friedman Lab.

²This F-P cavity is from the DeMille group at Yale University; it is also a confocal cavity with an athermal design. In fact, we borrowed the design for our F-P cavity from this model. As discussed in Chapter 2, this cavity has a higher finesse of above 1500 and an FSR of 500 MHz.

3.2 Supporting Theory

Sinusoidal modulation of the injection current causes sinusoidal response of the output electric field. Both amplitude and frequency modulation (AM and FM) result, and optical sidebands appear in the output of the laser.

3.2.1 $p - n$ Junctions

The main component of a laser diode is the $p - n$ junction. $p - n$ junctions are constructed by placing a p -doped semiconductor in contact with an n -doped semiconductor. The technique of creating these doped semiconductor materials is called doping, which adds impurity atoms to pure semiconductor materials such as silicon.

As Fig. 3.2 shows, the p -doped region has a lack of electrons, or equivalently a surplus of electron-holes; the holes in the valence band are mobile and ready to be combined with free electrons. In the n -doped region, there is a surplus of electrons; surplus electrons in the conduction band are ready to diffuse across the border to combine with mobile electron-holes. Note that even with a lack or surplus of electrons, the atoms in the two regions are neutral in charge.

Near the junction where the two types of material come in contact with each other, free electrons in the conduction band combine with the electron-holes in the valence band. Photons are emitted when the electrons combine with electron-holes, the energy of the released photon is

$$h\nu = E_c - E_v, \tag{3.1}$$

where h is Planck's constant, ν is the frequency of the emitted photons, E_c and E_v are

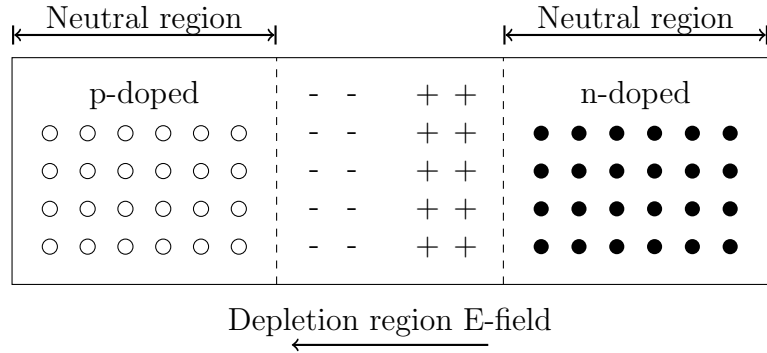


Figure 3.2: Illustration of a $p - n$ junction. Hollow circles represent electron holes while filled circles represent electrons. The area in between the dashed lines is the depletion region and the rest of the area remain neutral in charge.

the energy of the conduction and valence band, respectively. This energy difference, or the bandgap, is determined by the doped semiconductor material. Since there are many different energies in both the conduction and the valence band, the diode provides optical gain in a broad range of wavelengths/frequencies. The operation range of our Axcel laser diode (part number M9-940-0150-D5P) is from 935nm to 945nm.

As the free electrons combine with the mobile electron-holes, a depletion region is formed where a potential difference is developed across the border because the neutral atoms are now ionized. At equilibrium, the depletion region electric field stops more free electrons from combining with the holes. With an injection current, the n -doped region is constantly injected with free electrons. As a result, free electrons can combine with electron-holes to produce photons continually. [13, p 182-184]

$p - n$ junctions in laser diodes have a unique structure in which a thin layer of material is sandwiched between the two doped regions. Since the sandwiched layer is characterized by a larger refractive index than the surrounding regions due to

the choice of low-bandgap materials, the recombinations are confined within a small depletion region known as the active layer. [14, p 82] As injection current increases, an increasing number of electrons are confined to the active layer to allow stimulated emissions.

3.2.2 Radiative and Non-radiative Mechanisms

There are three mechanisms that simultaneously occur in a laser diode; an illustration of each of them is shown in Fig. 3.3. The valence band energy level has been taken as a ground state while the conduction band energy level can be seen as an excited state, as their relative energy level is more important in this discussion. Electron-holes in the active layer can absorb a resonant photon by raising to the excited state. Conversely, free electrons can spontaneously emit a photon corresponding to the energy difference of the two states. A photon with an energy equivalent to that of the band gap can also trigger an electron to combine with a hole, resulting in the stimulated emission of another photon with the same phase.

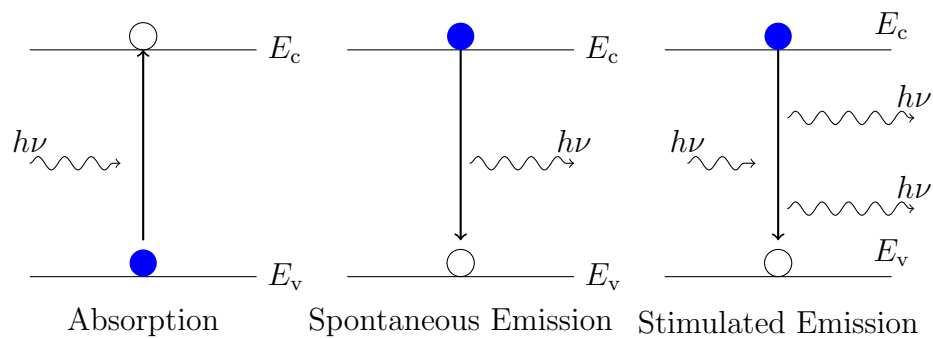


Figure 3.3: Illustration of stimulated emissions within an optical resonator.

Laser diodes rely on stimulated emissions to generate a coherent output because

stimulated emissions can quickly increase the number of photons that are in phase with each other. Stimulated emissions can only dominate once the electron density in the active layer exceeds a certain threshold called the transparency value. Beyond the threshold with a DC injection current, the net rate of stimulated emission per photon(G) is proportional to the number of electrons(N) in the active layer:

$$G = g(N - N_T), \quad (3.2)$$

where g is a constant and N_T is the number of electrons at transparency value. For a typical laser diode, the rate of spontaneous emission(R_{sp}) also varies linearly with G by a proportionality constant of around 2. [14, p 107]

Optical gain alone is not enough for laser operation. Remember that a laser diode also consists of an optical cavity formed by the two cleaved laser facets. The lasing threshold is met when optical gain exactly compensates for the cavity loss due to the imperfect reflectivity of the facets. The injection current needed to reach the threshold gain is called the threshold current(I_{th}).

3.2.3 The Rate Equations

For a single-mode laser diode, its dynamics follow a set of differential equations called the rate equations characterized by the photon number P and the electron number N [14, p 107] :

$$\frac{dP}{dt} = GP + R_{sp} - \frac{P}{\tau_p}, \quad (3.3)$$

$$\frac{dN}{dt} = \frac{I}{e} - GP - \frac{N}{\tau_c}. \quad (3.4)$$

In Eq. 3.3, the changes in photon count are determined by three terms: the net increase in photons emitted due to stimulated emissions, the generation of photons due to spontaneous emissions, and the net loss of photons determined by the lifetime τ_p of the photons. In Eq. 3.4, the changes in electron number are also determined by three terms: the first term gives the number of injected electrons obtained from dividing the injection current I by the elementary charge e , the second term takes into account the loss of electrons due to stimulated emissions, and the last term represents the loss of electrons due to both spontaneous emissions and nonradiative recombinations with τ_c as the carrier lifetime. Nonradiative recombinations refer to the recombinations of the electrons and holes that result in phonon emissions (i.e. semiconductor crystal lattice vibrations).

We are interested in solving the rate equations with a modulated injection current in the form of $I_b + I_m \cos \omega t$, where I_b is the DC bias current and I_m is the magnitude of the radio frequency modulation. As a pair of coupled differential equations, the rate equations can only be solved numerically. However, we can obtain an analytic solution by making the small signal approximation given that our modulation signal fulfills the following condition [14, p 110]:

$$I_m \ll I_b - I_{th}, \quad (3.5)$$

where I_{th} is the threshold current.

When the injection current is modulated, the net rate of stimulated emission per photon G is no longer linearly dependent on the number of electrons in the active layer

as described in Eq. 3.2. The following equation offers a more realistic description:

$$G = g(N - N_T)(1 - \epsilon_{NL}P), \quad (3.6)$$

where ϵ_{NL} is a non-linear gain parameter that is typically $\approx 10^{-7}$. This modified expression reflects the dependency of the gain on both the electron and photon number during injection current modulation.

With a small sine wave modulation, the rate equations can be linearized and solved using the small-signal approximation and the Fourier-transform technique to give a set of general solutions [15, p 84]:

$$P(t) = \langle P \rangle + \text{Re}[\Delta P e^{i\omega_m t}], \quad (3.7)$$

$$N(t) = \langle N \rangle + \text{Re}[\Delta N e^{i\omega_m t}]. \quad (3.8)$$

The number of electrons and photons vary sinusoidally around their mean values $\langle N \rangle$ and $\langle P \rangle$ at a frequency equivalent to the modulation frequency ω_m . To make this relationship a little more intuitive, one can take a look again at the rate equations. The injection current clearly affects the electron number from the second rate equation. The photon number is related to the injection current through G , which is related to both P and N according to Eq. 3.6.

Furthermore, given the modulated electron number in Eq. 3.8, the optical frequency ν is also directly modulated [15, p 121]:

$$\nu = \langle \nu \rangle + \text{Re}[\Delta \nu e^{i\omega_m t}], \quad (3.9)$$

where $2\pi\nu = \omega$. This result follows from the dependence of optical frequency on the refractive index and the group refractive index. Since the crystal surfaces of the active layer effectively serve as an optical resonator, the refractive index determines the possible emission frequencies and it changes rather linearly with electron numbers. On the other hand, the group refractive index concerns with the spacing between two adjacent emission frequencies (also called longitudinal mode spacing); it varies with the non-linear stimulated emission gain, which contributes to the non-linear modulation response of the optical frequency. [15, p 31-32]

While the electric field might be directly modulated in externally modulated systems, it is important to realize that the output power rather than the electric field is modulated during injection current modulation. [16] Therefore in our case,

$$P \propto |E(t)|^2, \quad (3.10)$$

where P is again the photon number and $E(t)$ is the electric field of the output optical wave. When deriving the electric field expressions for the optical sidebands in Sec. 3.2.6, this relationship will result in a square root for the electric field due to amplitude modulation.

Eq. 3.7 and Eq. 3.9 show that injection current modulation leads to both amplitude modulation and frequency modulation. It is in principle possible to predict the relative amount of AM vs. FM by solving the rate equations, but the diodes are typically not documented sufficiently for useful calculations. In practice, we can infer their relative strengths from the modulated sideband intensities.

3.2.4 The AM Theory

Before deriving the expression for optical sidebands, it is helpful to consider amplitude modulation and frequency modulation separately.

Consider a carrier wave $c(t)$ with frequency ω_c and amplitude A_c such that $c(t) = A_c \cos(\omega_c t)$. The amplitude of the carrier is modulated by the signal $s(t) = A_m \cos(\omega_m t)$, where A_m is the amplitude of the modulated signal and ω_m is the modulation frequency.

The effect of amplitude modulation is that the carrier amplitude at each moment is modified by the instantaneous value of the modulated signal. [17, p 94-96] In other words, the carrier amplitude is no longer constant: it is now $A_c + s(t)$. This new amplitude leads to a new expression for the modulated carrier wave:

$$c_{\text{AM}}(t) = [A_c + A_m \cos(\omega_m t)] \cos(\omega_c t). \quad (3.11)$$

Multiplying out each term within the parenthesis with $\cos(\omega_c t)$ and using trigonometric identities, Eq. 3.11 can be rewritten as

$$c_{\text{AM}}(t) = A_c \cos(\omega_c t) + \frac{A_m}{2} \cos(\omega_c - \omega_m)t + \frac{A_m}{2} \cos(\omega_c + \omega_m)t. \quad (3.12)$$

This equation shows that amplitude modulation with a single modulation frequency results in two sidebands (the second and third term in Eq. 3.12). Their amplitudes have the same signs and their frequencies differ from the carrier frequency by the modulation frequency.

3.2.5 The FM Theory

Frequency modulation is similar to phase modulation because both cause phase changes in the resulting output. Unlike phase modulation, which directly vary the phase of the carrier, in frequency modulation the phase change is a result of changes in the instantaneous frequency of the carrier. Consider the same sinusoidal carrier signal $c(t)$ from section 3.2.4, and the same modulation signal $s(t)$ except this time as frequency modulation. The instantaneous phase $\theta_{\text{FM}}(t)$ in frequency modulation is obtained by taking the integral of the modulation signal:

$$\theta_{\text{FM}}(t) = \omega_c t + \int_{t_0}^t s(t) dt, \quad (3.13)$$

where the lower integral limit is the time at the beginning of frequency modulation.

Since our modulation signal is a cosine wave, the instantaneous phase can be solved, and the modulated signal becomes

$$c_{\text{FM}}(t) = A_c \cos\left(\omega_c t + \frac{f}{\omega_m} \sin \omega_m t\right), \quad (3.14)$$

where f has units of angular frequency.

Unlike the case of amplitude modulation, Eq. 3.14 theoretically contains infinite sidebands when expanded into a Fourier series. The details of the expansion will soon be discussed along with injection current modulated sidebands.

3.2.6 Optical Sidebands

In Sec. 3.2.3 we established that under a small-signal modulation of the injection current, the output power and frequency respond sinusoidally. If we superpose a DC bias current I_b with an RF signal $I_m \cos \omega_m t$, making sure that $I_m \ll I_b - I_{th}$, the AM and FM theory derived in section 3.2.4 and section 3.2.5 are now ready to be applied.

Take the original electric field with just the bias current to be the carrier. The carrier can be written in complex exponential form for convenience: $E_0 e^{i\omega_0 t}$, where E_0 is the carrier amplitude and ω_0 is the carrier frequency. Here, the real part corresponds to the physical electric field. According to Eq. 3.11 and Eq. 3.14, the electric field resulting from each kind of modulation independently would be

$$E_{AM}(t) = E_0 e^{i\omega_0 t} \sqrt{(1 + M \cos \omega_m t)} \quad (3.15)$$

and

$$E_{FM}(t) = E_0 e^{i(\omega_0 t + \beta \sin \omega_m t)}, \quad (3.16)$$

respectively, where M is the degree of AM modulation and β is the FM modulation index. As mentioned before, the square root in Eq. 3.15 results from the output power instead of the electric field being directly modulated by the injection current.

Fourier expanding the frequency modulated electric field leads to the following

series[18]:

$$\begin{aligned}
E_0 e^{i(\omega_0 t + \beta \sin \omega_m t)} &= J_0(\beta) E_0 e^{i\omega_0 t} \\
&+ J_1(\beta) E_0 e^{i(\omega_0 t + \omega_m t)} - J_1(\beta) E_0 e^{i(\omega_0 t - \omega_m t)} \\
&+ J_2(\beta) E_0 e^{i(\omega_0 t + 2\omega_m t)} + J_2(\beta) E_0 e^{i(\omega_0 t - 2\omega_m t)} \\
&+ \dots \\
&+ J_l(\beta) E_0 e^{i(\omega_0 t + l\omega_m t)} + (-1)^l J_l(\beta) E_0 e^{i(\omega_0 t - l\omega_m t)}.
\end{aligned} \tag{3.17}$$

Each term in the series contains $J_l(\beta)$, or the Bessel functions of the first kind. The Bessel functions are functions of a single variable, in our case the modulation index β .

In Eq. 3.17, the first line refers to the carrier, the second line contains the first and minus first sidebands, and so on. Unlike amplitude modulation, sidebands due to pure frequency modulation are alternately in phase and out of phase.

The amplitudes of the carrier and the sidebands are determined by the Bessel functions. Fig. 3.4 shows the first three orders of the Bessel functions. As expected, with no modulation, $J_0(0)$ is unity and the carrier wave is at its full amplitude. For our experiments, we have $\beta < 1$ mostly because of the low rf power received by the laser diode. In this range, the amplitudes of the sidebands increase as β increases. Higher sidebands are suppressed due to the low amplitudes of the higher order Bessel functions.

Since modulating the injection current causes both amplitude and frequency modulation, combining Eq. 3.15 and Eq. 3.16 leads to the general modulated electric

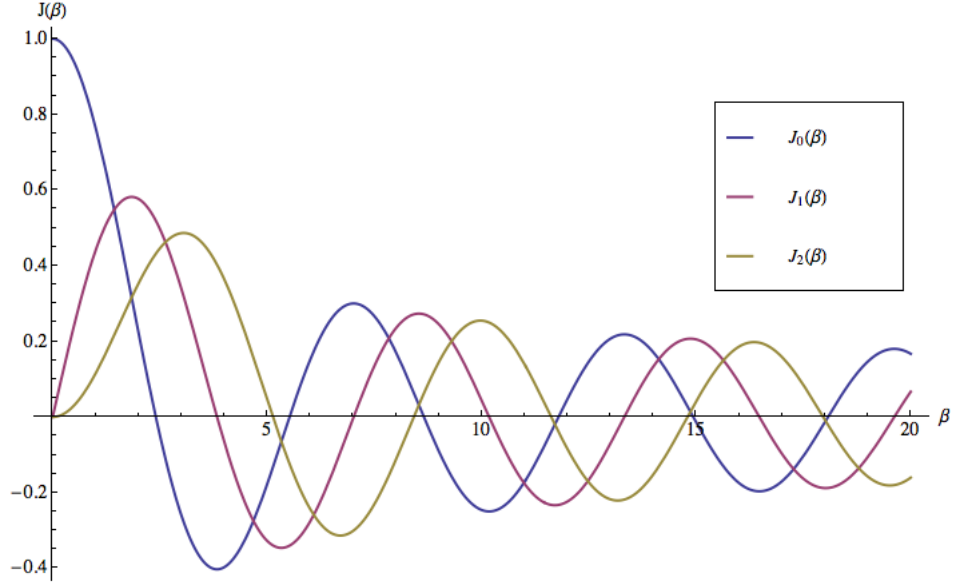


Figure 3.4: The first three orders of the Bessel functions.

field[16]:

$$E(t) = E_0 e^{i(\omega_0 t + \beta \sin \omega_m t)} \sqrt{1 + M \cos(\omega_m t)}. \quad (3.18)$$

This expression shows that the amplitudes of each pair of the frequency modulated sidebands are modified by amplitude modulation. A second order expansion of Eq. 3.18 gives an approximation of the first few sidebands:

$$\begin{aligned}
\text{Carrier} &: E_0 e^{i\omega_0 t} \left[J_0(\beta) \left(1 - \frac{M^2}{16}\right) - J_2(\beta) \frac{M^2}{16} \right]; \\
+1 &: E_0 e^{i(\omega_0 t + \omega_m t)} \left[J_0(\beta) \frac{M}{4} + J_1(\beta) \left(1 - \frac{M^2}{32}\right) + J_2(\beta) \frac{M}{4} \right]; \\
-1 &: E_0 e^{i(\omega_0 t - \omega_m t)} \left[J_0(\beta) \frac{M}{4} - J_1(\beta) \left(1 - \frac{M^2}{32}\right) + J_2(\beta) \frac{M}{4} \right]; \\
+2 &: E_0 e^{i(\omega_0 t + 2\omega_m t)} \left[-J_0(\beta) \frac{M^2}{32} + J_1(\beta) \frac{M}{4} + J_2(\beta) \left(1 - \frac{M^2}{16}\right) \right]; \\
-2 &: E_0 e^{i(\omega_0 t - 2\omega_m t)} \left[-J_0(\beta) \frac{M^2}{32} - J_1(\beta) \frac{M}{4} + J_2(\beta) \left(1 - \frac{M^2}{16}\right) \right].
\end{aligned} \quad (3.19)$$

These expressions are derived in Appendix A.

Further reducing Eq. 3.19 by ignoring terms containing M^2 gives a set of simpler expressions:

$$\begin{aligned}
\text{Carrier} &: E_0 e^{i\omega_0 t} J_0(\beta); \\
+1 &: E_0 e^{i(\omega_0 t + \omega_m t)} \left[J_0(\beta) \frac{M}{4} + J_1(\beta) + J_2(\beta) \frac{M}{4} \right]; \\
-1 &: E_0 e^{i(\omega_0 t - \omega_m t)} \left[J_0(\beta) \frac{M}{4} - J_1(\beta) + J_2(\beta) \frac{M}{4} \right]; \\
+2 &: E_0 e^{i(\omega_0 t + 2\omega_m t)} \left[J_1(\beta) \frac{M}{4} + J_2(\beta) \right]; \\
-2 &: E_0 e^{i(\omega_0 t - 2\omega_m t)} \left[-J_1(\beta) \frac{M}{4} + J_2(\beta) \right].
\end{aligned} \tag{3.20}$$

This set of approximations differ from the ones derived from directly modulating the electric field instead of the power by a factor of 1/2 in the terms related to amplitude modulation.[18]

Since a photodetector measures intensity rather than electric field, the relative intensity of each sideband can be obtained by taking the absolute value squared of the respective electric field and dividing by the absolute value squared of the carrier electric field. Experimental observations of any two sideband intensities relative to that of the carrier will be sufficient for solving both β and M .

3.3 Experimental Observations

According to Sec. 3.2.6, first sidebands have a frequency of $f_0 + f_m$ while minus first sidebands have a frequency of $f_0 - f_m$, where f_0 is the carrier frequency and f_m is the modulation frequency. Fig. 3.5 shows the transmission peak positions as

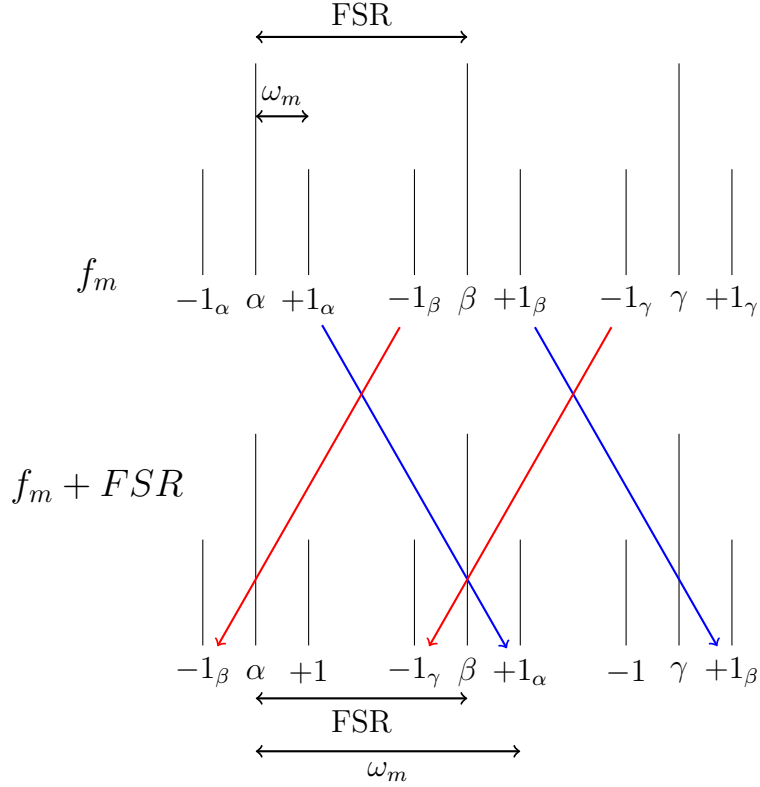


Figure 3.5: An illustration of sideband positions for different modulation frequencies. α , β , γ denote carrier peaks as we scan the F-P cavity, the distance between adjacent carriers is the FSR. $+1$ and -1 are first and minus first sidebands and their subscripts indicate the corresponding carriers. The sidebands are separated from the corresponding carriers by the modulation frequency.

we scan the F-P cavity by more than two FSRs. Notice that when we increase the modulation frequency by one FSR, some sidebands ($+1_\gamma$ and -1_α) are off the screen. We still see the same sideband pattern because sidebands from other carriers fill in their positions. This analysis demonstrates that the F-P cavity registers the same pattern for modulation frequencies that differ by an integer number of the FSR.

Since the first and minus first sidebands are symmetrically spaced with respect to the carrier, they overlap for f_m at integer multiples of 250 MHz if our cavity FSR

is actually 500 MHz. This allows us to measure the FSR of our cavity by observing the modulation frequency for which the first and minus first sidebands overlap. In Fig. 3.6, the first and minus first sidebands overlap exactly for $f_m = 2750$ MHz, confirming that our FSR is 500 MHz.

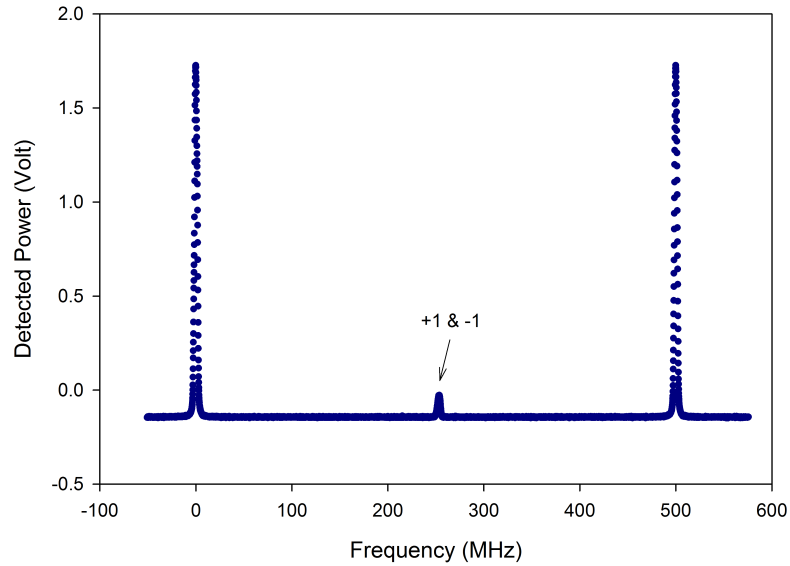


Figure 3.6: Sidebands modulated at 2750 MHz. The first and minus first sidebands coincide at the center between two carrier peaks.

Fig. 3.7 shows another observation that is consistent with theoretical predictions. We mentioned in Sec. 3.2.4 that injection current modulation results in both AM and FM. The AM modulation causes uneven power in the first and minus first sidebands, which is evident in Fig. 3.7. Also note that the power of negative sidebands is always less than that of positive sidebands according to the expanded expressions for the sidebands in Sec. 3.2.6.

Now that we know our setup works, recall that our goal is two-fold: we want to

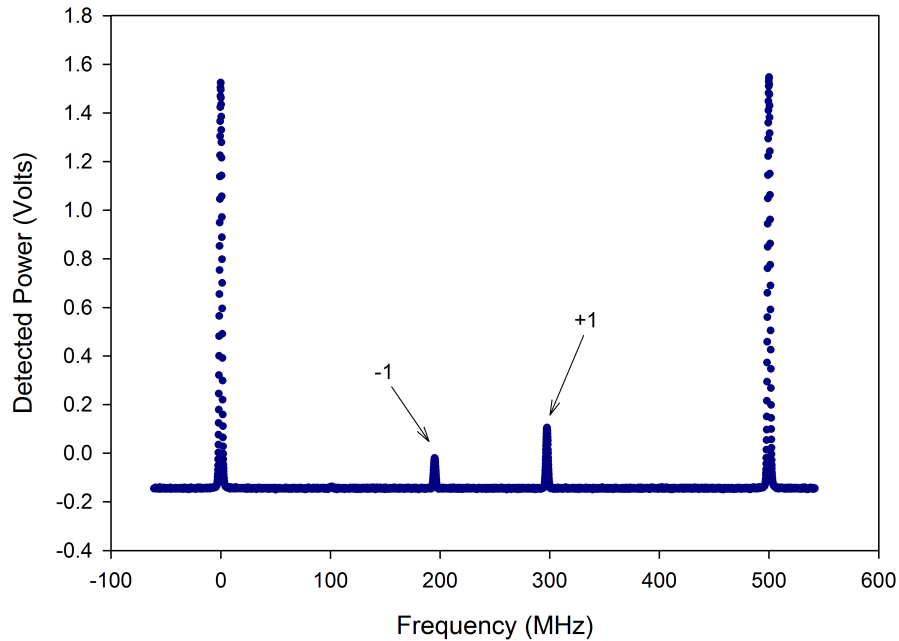


Figure 3.7: First sidebands produced by direct injection current modulation at 4300 MHz. The bias current is at 25mA and the rf signal generator output is 20dBm.

maximize the modulation frequency and improve modulation response (i.e. higher sideband powers). We identify general trends in modulation response and examine the various relevant factors in order to find the optimal condition for our system.

3.3.1 General Decline with Increasing Modulation Frequency

Modulation response generally declines with increasing modulation frequency.[18] There are two possible factors for this phenomenon. The first one is based on the inverse relationship between modulation index β and modulation frequency ω_m :

$$\beta = \frac{2\pi\Delta F}{\omega_m}, \quad (3.21)$$

where ΔF is the maximum frequency deviation.[19] Note that ω_m in the denominator results from integrating Eq. 3.14. For small β (< 1), higher order Bessel functions decrease with β (see Fig. 3.4); the sideband powers decrease with the higher order Bessel functions.

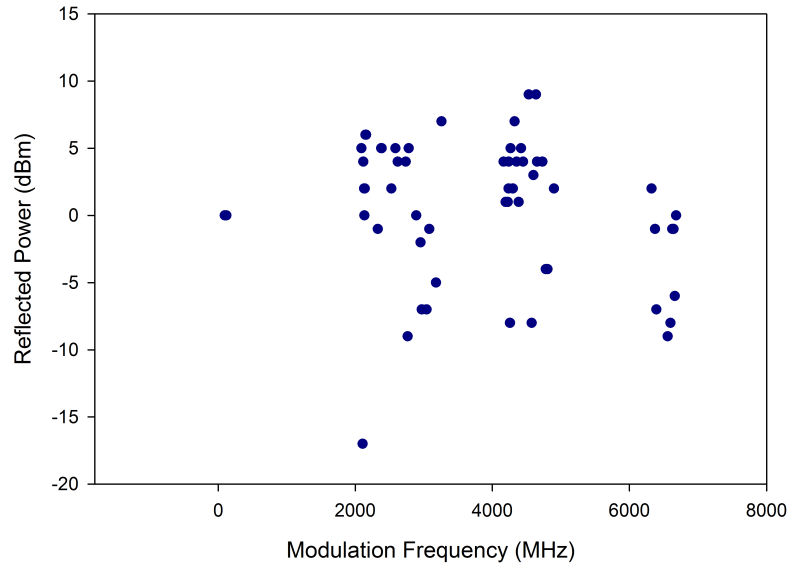


Figure 3.8: The reflected rf power as measured by the crystal detector for 20dBm rf input power. The -16dBm attenuation due to the directional coupler is accounted for in the plot.

The second factor is associated with experimental practice. In our current setup, the rf power can be seriously attenuated at high frequencies because we did not impedance-match the rf power. In fact, there has been accounts of at least a 50% reduction in the rf power received by the laser diodes in similar experiments. [11, 19]

We monitor the rf power reflected off our laser diode with a directional coupler. The signal is measured by a crystal detector and recorded for select frequencies in Fig. 3.8. The rf signal input is 20dBm for all the reflected powers recorded in Fig. 3.8.

Surprisingly, only as much as 10% of the incident power is reflected back. However, given the amount of modulation we observe in the sidebands, it is unlikely that all of the remaining power goes into the laser diode. One way to potentially increase the rf power received by the laser diode is to increase the incident rf power. Unfortunately, the rf signal output in our setup cannot exceed 20dBm. For future experiments, it might be helpful to use an rf generator with higher output power.

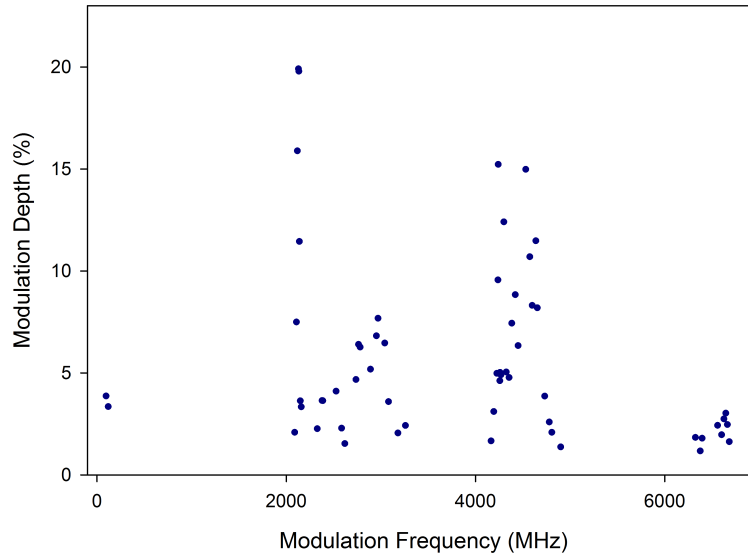


Figure 3.9: First sidebands modulation depths at different modulation frequencies for DC bias at 55mA. We were only able to observe sidebands at modulation frequencies corresponding to the data points plotted in this figure.

We observe the relative power of the first and minus first sidebands with respect to the carrier (i.e. the modulation depth) for various modulation frequencies. The modulation depths for the first sidebands are plotted in Fig. 3.9. Using the expressions for the carrier, first sidebands, and minus first sidebands from Sec. 3.2.6, we can calculate the AM and FM modulation indices. The results are plotted in Fig. 3.10.

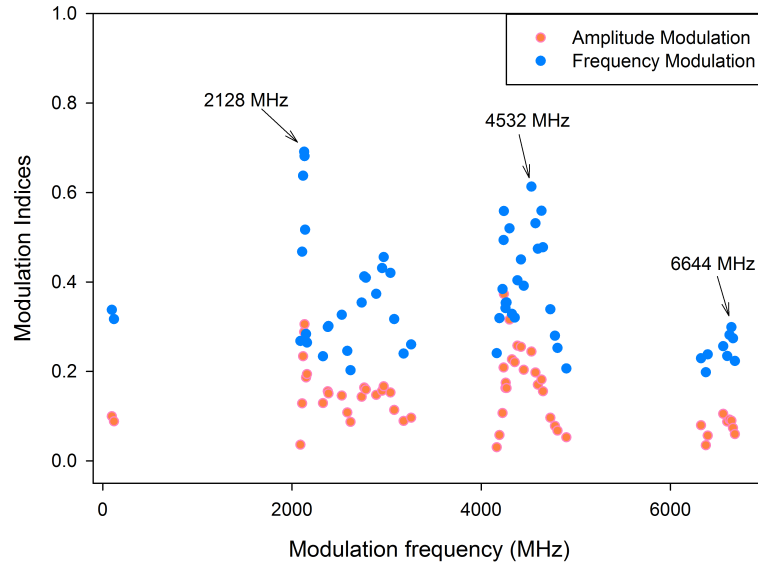


Figure 3.10: FM indices(β) and AM indices(M) for modulation frequencies from 15-6650 MHz. The DC bias current is at 55mA for all data points. Note that missing data points correspond to β and $M \sim 0$ at those modulation frequencies.

In Fig. 3.10 and Fig. 3.9, the peak heights decline with increasing frequency, supporting the discussion above. The exception at around 100 MHz and the dramatic response at certain frequencies are due to another phenomenon discussed in the following section.

3.3.2 Dramatic Improvements from External Cavity Feedback

Because of the constructive feedback provided by the external cavity in an ECDL, there is a strong correlation between modulation response and the free spectral range (FSR) of the external cavity.[18–20] More specifically, optimal modulation depth is

achieved with f_m at integer multiples of the external cavity FSR.

This dramatic improvement in modulation response is prominent in Fig. 3.10 and Fig. 3.9. Although in the previous section we discussed about reduced modulation responses at higher modulation frequencies, the cavity feedback allows better modulation responses at 2 GHz and at 4.5 GHz than those at sub-FSR frequencies.

Because Fig. 3.10 and Fig. 3.9 are quite noisy, which might be partly because of the fluctuations in the rf power, we cannot extrapolate from them with much precision our actual external cavity FSR. Nonetheless, since the modulation responses peak consistently below the expected frequencies for the FSR at 2.4 GHz, 2.2 GHz is probably a better estimate.

3.3.3 Bias Current Dependence

There have been several observations of improved modulation response upon decreasing the bias current.[11, 19, 20] In some cases, the modulation depths are quite sensitive to how far the current is above threshold. [11]

There are two possible explanations for this phenomenon. First, when decreasing the bias current (while still remaining above the threshold current), the fractional modulation amplitude given the same rf power increases. This leads to an increase in β , which improves modulation response.

Second, the parasitic capacitance in laser diodes might filter out high frequency rf signals.[15, p 93-94] As a potential develops between the two doped semiconductor regions (explained in Sec. 3.2.1), the $p - n$ junction becomes analogous to a parallel plate capacitor. If we approximate a laser diode as a diode connected in parallel with a capacitor, the laser diode becomes effectively a low-pass filter. Lowering the DC

bias current can reduce the parasitic capacitance and allow higher frequency rf signals to enter the diode, improving the modulation response.

We vary the bias current at $f_m = 4300$ MHz and at $f_m = 6644$ MHz, where we observed maximum modulation response according to Fig. 3.10. Since our laser current threshold is 18mA, we start the bias current at 20mA. For $f_m = 4300$ MHz, Fig. 3.12 and Fig. 3.11 show that modulation response generally decays as we increase the bias current. There is a local maximum around 55mA for both AM and FM indices, and the corresponding modulation depth is around 10 %.

At $f_m = 6644$ MHz, Fig. 3.13 and Fig. 3.11 indicate maximum modulation response at around 50mA. There is a greater bias current dependence of the AM indices than the FM indices. While modulation response almost linearly increases with de-

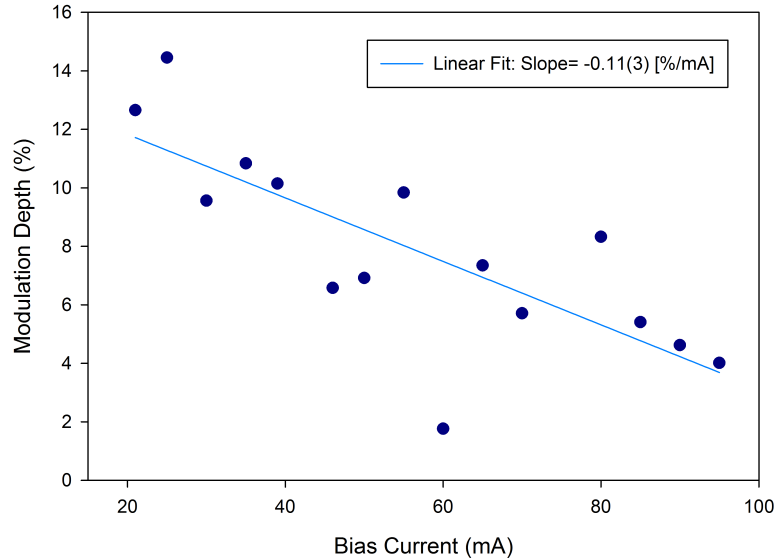


Figure 3.11: Bias current dependence of modulation depth at $f_m = 4300$ MHz. Linear fit slope is attached.

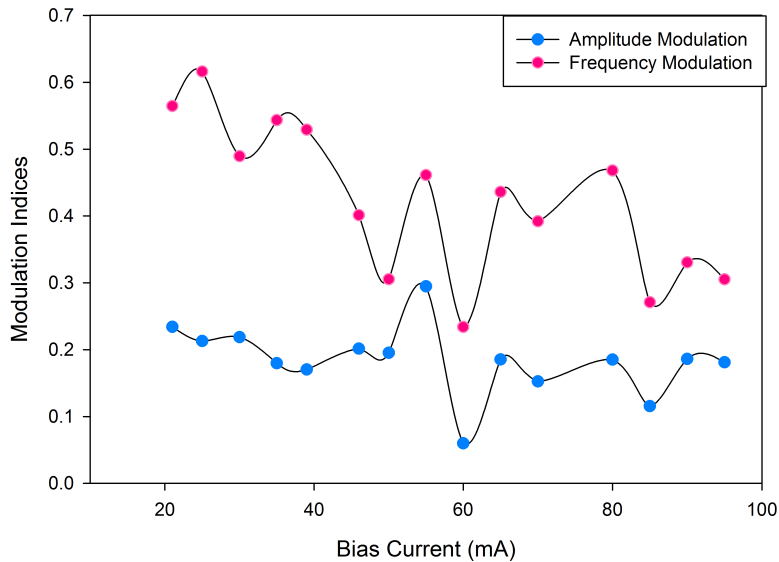


Figure 3.12: Bias current dependence of modulation indices at $f_m = 4300$ MHz.

creasing bias current for $f_m = 4300$ MHz, at $f_m = 6644$ MHz the modulation response declines both at low and high bias currents. We attempt to explain this difference in the following section.

3.3.4 Frequency of Oscillation Relaxations

There is an upper limit on modulation frequency for each laser diode. This is determined by the frequency of relaxation oscillations, which is related to how fast the laser diode can return to its steady-state under current disturbances. In general, modulation efficiency decreases dramatically as the modulation frequency increases far above the frequency of relaxation oscillations. [14, p 144]

The frequency of relaxation oscillations in some diode lasers has been documented to range from 2 to 5 GHz. [14, p 210] In our case, we were not able to observe any

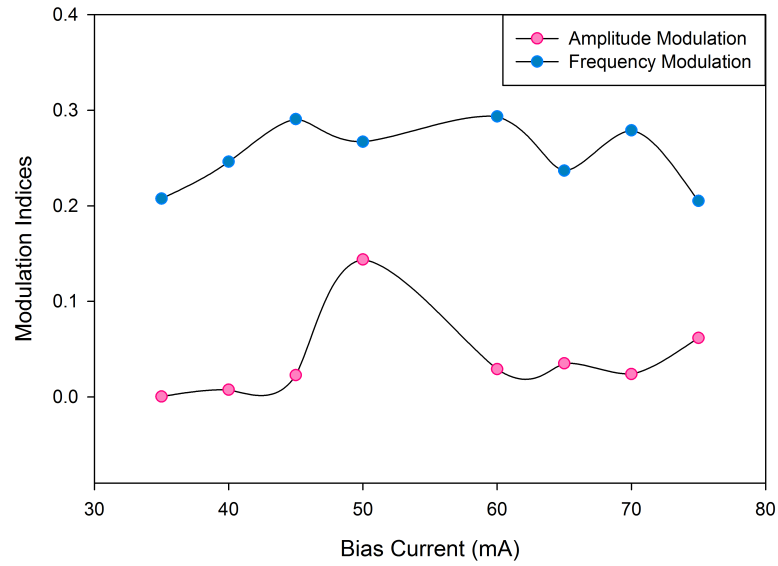


Figure 3.13: Bias current dependence of modulation indices at $f_m = 6644$ MHz.

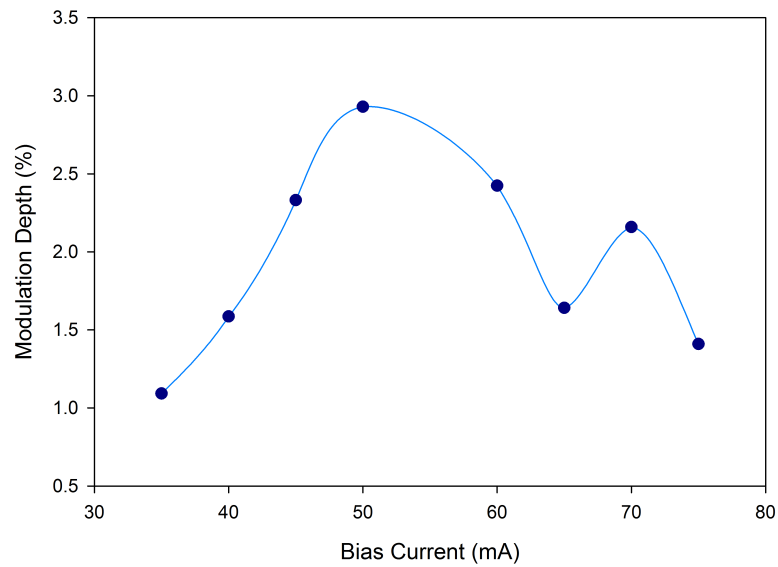


Figure 3.14: Bias current dependence of modulation depth at $f_m = 6644$ MHz.

sidebands after 6650 MHz. The next external cavity feedback is at least above 8 GHz, which might exceed the frequency of oscillation relaxations by too much to allow for any modulation response.

We have mentioned the improved modulation responses with lower bias current. This improvement is counteracted, however, by the dependence of the frequency of relaxation oscillations (f_r) on the bias current (I). This relationship is expressed in the following equation:

$$f_r = \sqrt{\frac{I/I_{th} - 1}{\tau_c \tau_p}}, \quad (3.22)$$

where I_{th} is the threshold current, τ_c and τ_p are the carrier and photon lifetimes, respectively.[19]

Eq. 3.22 might explain the difference in the bias current dependence of modulation responses observed for 4300 MHz and 6644 MHz (compare Fig. 3.11 and Fig. 3.14). As the bias current decreases, f_r also decreases, lowering the the upper limit of the modulation frequency. Hence we observe a decline in modulation response for 6644 MHz at low bias currents. For bias current at 50mA, we obtain 3% modulation depth for the first sidebands at $f_m = 6.6$ GHz. Without considering the absolute powers of the carrier and the sidebands, this seems to be the optimal condition for our system.

3.3.5 Mysterious Sidebands

So far we have examined observations that are consistent with theoretical expectations. We also encountered a puzzling situation where unexpected sidebands appear at $0.5f_m$ away from the carrier frequency. These “half sidebands” persist between $f_m = 4243$ MHz and $f_m = 4309$ MHz. While the theory only predicts integer side-

bands, the “half-sidebands” in Fig. 3.15 appear AM and FM modulated.

We also found that at $f_m = 4266$ MHz, the diode is destabilized. Perhaps there is a connection between these two phenomena, but we have not yet found an explanation for it.

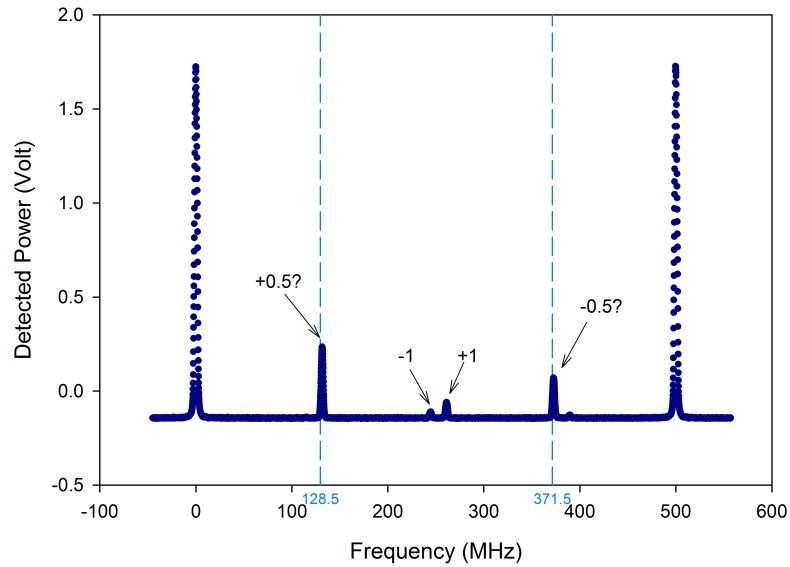


Figure 3.15: Sidebands modulated at 4257 MHz. The dashed lines mark the positions of the hypothetical “half sidebands”.

While these “half sidebands” are unexpected, they are not serious concerns given what we need. We have demonstrated that our diode laser can be modulated up to 6.6 GHz and that its relative power with respect to the carrier can be adjusted with the DC current. The power in the optical sideband is likely enough if we use them as resonant beams so that the non-resonant (Raman) beams can benefit from the larger power of the carrier. Hopefully, the detuning generated using injection current modulation is large enough for Raman transitions.

Chapter 4

Conclusion

We have built a laser lock that automates frequency stabilization. According to a thallium fluoride molecular transition, the system is stable to within 200 kHz over 3 hours. Since the system depends on the stability of the Fabry-Perot cavity, we took measures to isolate the cavity from acoustic vibrations and pressure and temperature variations. We showed that our system is resistant to temperature changes below 0.6°C. For usual lab temperature drifts, our system is practically athermal. This setup is complete and mounted on a 1' × 2' mobile breadboard, designed to be conveniently incorporated into laser systems with fiber-coupled outputs. We have used this laser lock to successfully stabilize the frequency of our external cavity diode laser.

For injection current modulation, we have demonstrated that our ECDL can be most effectively modulated at frequencies around 2.2 GHz, 4.4 GHz, and 6.6 GHz due to the enhanced external cavity feedback. We observed a strong correlation between the modulation response and the bias current. At 6.6 GHz, the optimal bias current

is at 50mA, where we obtain 3 % of the output power in the sideband. Although we had originally hoped to modulate the laser diode at 9.6 GHz, we believe that a 6.6 GHz detuning could also allow us to implement Raman transitions for the sideband cooling. Its efficiency of course awaits to be tested on the logic ions.

An immediate next step is to convert both the carrier and the sideband to the ultraviolet. Celia Ou has designed a frequency conversion setup and it is still in the construction stage. After frequency conversion, the carrier and the sideband need to be modulated by acousto-optic modulators to generate a total of 6 laser beams. The carrier will be modulated to produce the two Raman beams separated by around 1.25 GHz. The sideband will be the source of the Doppler beams, repump laser, and detection laser. Once the logic ions are trapped, these six beams can potentially accomplish the second step we mentioned in Chapter 1, preparing the logic ions for manipulating the spectroscopy ions.

Appendix A

Optical Sideband Derivations

The goal is to expand

$$E(t) = E_0 e^{i(\omega_0 t + \beta \sin \omega_m t)} \sqrt{1 + M \cos(\omega_m t)}. \quad (\text{A.1})$$

The following expansions are taken from ref. [21]:

$$(1 + x)^\alpha = 1 + \alpha x + \frac{\alpha(\alpha - 1)}{2!} x^2 + \frac{\alpha(\alpha - 1)(\alpha - 2)}{3!} x^3 + \dots + \binom{\alpha}{n} x^n, \quad (\text{A.2})$$

where the interval of convergence is $-1 < x < 1$.

$$\cos^{2n} x = \frac{1}{2^{2n-1}} \sum_{k=0}^{n-1} \binom{2n}{k} \cos(2n - 2k)x + \binom{2n}{n} \frac{1}{2^{2n}} \quad (\text{A.3})$$

and

$$\cos^{2n-1} x = \frac{1}{2^{2n-2}} \sum_{k=0}^{n-1} \binom{2n-1}{k} \cos(2n - 2k - 1)x. \quad (\text{A.4})$$

Since we are modulating the injection current with a small signal, assume $|M| < 1$

and the square root term in Eq. A.1 can be rewritten as

$$1 + \frac{1}{2}M \cos(\omega_m t) - \frac{1}{8}M^2 \cos^2(\omega_m t) + \frac{1}{16}M^3 \cos^3(\omega_m t) + \dots + \sum_n^{\infty} \binom{\frac{1}{2}}{n} M^n \cos^n(\omega_m t). \quad (\text{A.5})$$

Expanding the first few terms of Eq. A.5 using Eq. A.3 and Eq. A.4 leads to

$$\begin{aligned} & 1 + \frac{1}{2}M \cos(\omega_m t) \\ & - \frac{1}{16}M^2 - \frac{1}{16}M^2 \cos(2\omega_m t) \\ & + \frac{1}{64}M^3 \cos(3\omega_m t) + \frac{3}{64}M^3 \cos(\omega_m t) \\ & + \dots \end{aligned} \quad (\text{A.6})$$

For convenience, cosines can also be written in complex exponential form so that the first three lines of Eq. A.6 become

$$\begin{aligned} & 1 + \frac{1}{4}M e^{i\omega_m t} + \frac{1}{4}M e^{-i\omega_m t} \\ & - \frac{1}{16}M^2 - \frac{1}{32}M^2 e^{2i\omega_m t} - \frac{1}{32}M^2 e^{-2i\omega_m t} \\ & + \frac{1}{128}M^3 e^{3i\omega_m t} + \frac{1}{128}M^3 e^{-3i\omega_m t} + \frac{3}{128}M^3 e^{i\omega_m t} + \frac{3}{128}M^3 e^{-i\omega_m t}. \end{aligned} \quad (\text{A.7})$$

Recall from Chapter 3 that using Fourier expansion,

$$\begin{aligned}
e^{i(\omega_0 t + \beta \sin \omega_m t)} &= J_0(\beta) E_0 e^{i\omega_0 t} \\
&+ J_1(\beta) E_0 e^{i(\omega_0 t + \omega_m t)} - J_1(\beta) E_0 e^{i(\omega_0 t - \omega_m t)} \\
&+ J_2(\beta) E_0 e^{i(\omega_0 t + 2\omega_m t)} + J_2(\beta) E_0 e^{i(\omega_0 t - 2\omega_m t)} \\
&+ \dots \\
&+ J_l(\beta) E_0 e^{i(\omega_0 t + l\omega_m t)} + (-1)^l J_l(\beta) E_0 e^{i(\omega_0 t - l\omega_m t)},
\end{aligned} \tag{A.8}$$

where $J_l(\beta)$ is the l th order Bessel function of the first kind.

Combining Eq. A.7 and Eq. A.8 and neglecting all terms smaller than M^2 gives the second order expansion of the first few sidebands:

$$\begin{aligned}
\text{Carrier} &: E_0 e^{i\omega_0 t} \left[J_0(\beta) \left(1 - \frac{M^2}{16} \right) - J_2(\beta) \frac{M^2}{16} \right]; \\
+1 &: E_0 e^{i(\omega_0 t + \omega_m t)} \left[J_0(\beta) \frac{M}{4} + J_1(\beta) \left(1 - \frac{M^2}{32} \right) + J_2(\beta) \frac{M}{4} \right]; \\
-1 &: E_0 e^{i(\omega_0 t - \omega_m t)} \left[J_0(\beta) \frac{M}{4} - J_1(\beta) \left(1 - \frac{M^2}{32} \right) + J_2(\beta) \frac{M}{4} \right]; \\
+2 &: E_0 e^{i(\omega_0 t + 2\omega_m t)} \left[-J_0(\beta) \frac{M^2}{32} + J_1(\beta) \frac{M}{4} + J_2(\beta) \left(1 - \frac{M^2}{16} \right) \right]; \\
-2 &: E_0 e^{i(\omega_0 t - 2\omega_m t)} \left[-J_0(\beta) \frac{M^2}{32} - J_1(\beta) \frac{M}{4} + J_2(\beta) \left(1 - \frac{M^2}{16} \right) \right].
\end{aligned} \tag{A.9}$$

Appendix B

Allan Deviation

The following is the Mathematica code used to calculate Allan deviations.

```
allanDev = {};  
bins = channelA;  
For[a = 1, a <= (Length[channelA] / 2), a++, {  
  bins = Partition[channelA, a];  
  AppendTo[allanDev, Join[  
    {2 a, Sqrt[Sum[(Mean[bins[[i]]) - Mean[bins[[i - 1]])]^2,  
      {i, 2, Length[bins]}] / (2 (Length[bins] - 1))}]]]]
```

channelA is the list containing the frequency measurements over the 3 hours. Our goal is to obtain a list of Allan deviations corresponding to each time scale; we call this list **allanDev**.

The *Partition*[*list*, *n*] function in Mathematica partitions the given *list* into nonoverlapping sublists of length *n*. We name the collection of sublists resulting from the partition of channelA **bins**.

The loop successively partitions channelA into bins containing less and less data points. At each step, the loop calculates the Allan deviation with the **Sqrt[...]** term. The loop starts from having 1 bin and stops at a bin number corresponding to 2 data points in each bin. I use the **Join[...]** function to time-stamp each calculated Allan deviation using the fact that each measurement took 2 seconds. The resulting allanDev is a list containing Allan deviations(MHz) vs. time(s).

Bibliography

- [1] J.-P. Uzan, “The Fundamental Constants and Their Variation: Observational Status and Theoretical Motivations,” *Rev.Mod.Phys.* (2002).
- [2] S. Qiao, “Constructing a Linear Paul Trap System for Measuring Time-variation of the Electron-Proton Mass Ratio,” Amherst College Undergraduate Thesis (2013).
- [3] C. Ou, “Third Harmonic Conversion,” Amherst College Undergraduate Thesis (2013).
- [4] R. B. Blakestad, *Transport of Trapped-Ion Qubits within a Scalable Quantum Processor*, Ph.D. thesis, University of Colorado (2010).
- [5] D. Wineland, M. Barrett, J. Britton, J. Chiaverini, B. DeMarco, W. Itano, B. Jelenkovic, C. Langer, D. Leibfried, V. Meyer, T. Rosenband, and T. Schatz, “Quantum Information Processing with Trapped Ions,” *Phil. Trans. Royal Soc. London A* (2003).
- [6] J. T. Verdeyen, *Laser Electronics* (Prentice-Hall, Inc., New York, 1981).

- [7] D. C. Sinclair, “Scanning Spherical-Mirror Interferometers For The Analysis of Laser Mode Structure,” Spectra-Physics laser Technical Bulletin (1968).
- [8] S. D. Saliba, M. Junker, L. D. Turner, and R. E. Scholten, “Mode Stability of External Cavity Diode Lasers,” Optical Society of America (2009).
- [9] N. S. Wadia, “Measurements of Branching Ratios for the B(0)-X(ν) Transition in Thallium Fluoride to Determine its Potential for Laser Cooling,” Amherst College Undergraduate Thesis (2013).
- [10] B. Hemmerling, F. Gebert, Y. Wan, and D. Nigg, “A single laser system for ground-state cooling of $^{25}\text{Mg}^+$,” Applied Physics B (2011).
- [11] C. J. Myatt, N. R. Newbury, and C. E. Wieman, “Simplified Atom Trap By Using Direct Microwave Modulation Of A Diode Laser,” Optics Letters **18**, 649 (1993).
- [12] R. Kowalski, S. Root, S. D. Gensemer, and P. L. Gould, “A Frequency-Modulated Injection-Locked Diode Laser For Two-Frequency Generation,” Review of Scientific Instruments **72**, 2532 (2001).
- [13] W. T. Silfvast, *Laser Fundamentals* (Prentice-Hall, Inc., Cambridge, 2004).
- [14] G. P. Agrawal, *Fiber-Optic Communication Systems* (John Wiley and Sons, Inc., 2002), 2nd ed.
- [15] K. Petermann, *Laser Diode Modulation and Noise* (Springer Netherlands, 1998).
- [16] X. Zhu and D. T. Cassidy, “Modulation Spectroscopy With A Semiconductor

- Diode Laser By Injection-Current Modulation,” *Optical Society of America* **14**, 1945 (1997).
- [17] L. E. Frenzel, *Principles of Electronic Communication Systems* (McGraw-Hill Science/Engineering/Math, 2007), 3rd ed.
- [18] A. Waxman, M. Givon, G. Aviv, D. Groswasser, and R. Folman, “Modulation Enhancement of A Laser Diode In An External Cavity,” *Applied Physics B* **95**, 301 (2009).
- [19] P. N. Melentiev, M. V. Subbotin, and V. I. B. Balykin, “Simple and Effective Modulation of Diode Lasers,” *Laser Physics* **11**, 1 (2001).
- [20] J. Ringot, Y. Lecoq, J. C. Garreau, and P. Szniftgiser, “Generation of Phase-Coherent Laser Beams for Raman Spectroscopy and Cooling by Direct Current Modulation,” *The European Physical Journal D* **7**, 285 (1999).
- [21] L. Rade and B. Westergren, *Beta Mathematics Handbook* (CRC Press, 1992), 2nd ed.